https://doi.org/10.5194/egusphere-2026-3792
Preprint. Discussion started: 21 July 2026

Constraining 2020 methane emissions in the Eastern Mediterranean and Middle East using TROPOMI satellite data

Martin Vojta[1,2], Rakesh Subramanian[1], Nikos Gialesakis[2,3], Rona L. Thompson[4], Andreas Stohl[1], and Maria Kanakidou[2]

[1]Department of Meteorology and Geophysics, University of Vienna, Vienna, Austria
[2]Department of Chemistry, Environmental Chemical Processes Laboratory (ECPL), University of Crete, Crete, Greece
[3]Institute of Environmental Physics, Laboratory for Modeling and Observation of the Earth System (LAMOS), and Center for Marine Environmental Sciences (MARUM), University of Bremen, Bremen, Germany
[4]NILU, Kjeller, Norway

Correspondence: Martin Vojta (martin.vojta@univie.ac.at)

Abstract.

Methane (CH_4) is the second most abundant anthropogenic greenhouse gas after CO_2. Emissions from the Eastern Mediterranean and Middle East (EMME) are of particular relevance, as the region hosts a large share of global oil and gas production and thus offers significant mitigation potential. In this study, we use TROPOMI satellite observations in combination with the Lagrangian particle dispersion model FLEXPART and the inversion framework FLEXINVERT+ to estimate CH_4 emissions in the EMME region for 2020. We perform sensitivity experiments to address methodological challenges and better quantify emission uncertainties.

Our inversions show robust downward corrections of emissions around the Persian Gulf relative to the EDGAR v8.0 inventory, consistent with the recently released EDGAR_2025_GHG dataset, yielding total emissions of 22.4 ($\pm$1.9) Tg yr^{-1} in the EMME region. At the national scale, we derive emissions of 4.6 ($\pm$0.4), 3.6 ($\pm$1.1), 3.5 ($\pm$0.8), 2.8 ($\pm$0.4), and 1.9 ($\pm$0.4) Tg yr^{-1} CH_4 for Iran, Saudi Arabia, Turkey, Iraq, and Egypt, respectively. While many countries in the region appear to substantially underestimate their emissions, Greece, subject to mandatory reporting requirements, reports emissions comparable to our inversion estimates. Our results further suggest a decrease in emissions in the EMME region during 2020, coinciding with reduced oil demand during the COVID-19 epidemic.

Our satellite-based inversions provide robust constraints in regions with strong emission signals and good observational coverage (e.g. Iran, Iraq), while other regions show greater sensitivity to uncertainty settings and a priori estimates. Our sensitivity analyses highlight the importance of baseline optimization and its associated uncertainty.

1 Introduction

The emissions-based effective radiative forcing attributable to CH_4 contributed roughly 31% of the total forcing from anthropogenic GHG emissions and their precursors over the industrial era (Forster et al., 2021), second only to carbon dioxide (CO_2). CH_4 has a Global Warming Potential (GWP) of 29.8 for fossil sources and 27.0 for non-fossil sources over a 100-year horizon,

https://doi.org/10.5194/egusphere-2026-3792
Preprint. Discussion started: 21 July 2026

rising to 82.5 and 79.7, respectively, over a 20-year time span (Szopa et al., 2021). Its relatively short atmospheric lifetime of about 9.25 years (Szopa et al., 2021) makes CH_4 a crucial target for mitigating near-term warming. Atmospheric CH_4 mole fractions are currently about 2.6 times higher than its estimated pre-industrial levels. Following strong growth in the 1990s, mole fractions stabilized in the early 2000s (e.g. Rigby et al., 2008), before increasing again since 2006 (Lan et al., 2025). This increase is driven by anthropogenic emissions from agriculture, fossil fuel extraction and use, waste management, and alterations to natural CH_4 fluxes (Saunois et al., 2025).

Anthropogenic sources account for roughly two-thirds of global CH_4 emissions, and approximately one-third of these are associated with fossil fuel production, of which 56% are attributed to oil and gas activities (Saunois et al., 2025). CH_4 emissions in the oil sector originate mainly from venting of associated gas, incomplete combustion during flaring, and activities related to transport and refining, while in the gas sector, emissions occur throughout the life cycle, primarily as fugitive emissions and during flaring (IEA, 2024). The oil and gas sector is of particular relevance, as it represents the greatest potential for low-cost CH_4 mitigation, supported by many readily applicable and technologically feasible solutions (Nisbet et al., 2020; Ocko et al., 2021).

A large fraction of global oil and gas extraction occurs in the Eastern Mediterranean and Middle East region[1] (EMME). The Middle East represents a key region for mitigating CH_4 emissions accounting for approximately one-third of the world's oil production and approximately one-sixth of the global natural gas supply (IEA, 2021). Hotspots are concentrated around the Persian Gulf and its coastal areas, which host a large number of oil and gas fields. Another emission hotspot is the Gulf of Suez (Bourtsoukidis et al., 2024), while high levels of CH_4 mole fractions have also been observed over the Suez Canal and the Red Sea, primarily linked to nearby oil and gas activities (Paris et al., 2021). In the eastern Mediterranean, significant gas fields have been discovered in the Nile Delta (Cozzi et al., 2021) and the Levantine Sea (Karcz et al., 2019).

However, emission estimates for the oil and gas sector are highly uncertain due to the large number of point sources involved, ranging from large, high-impact sites (Irakulis-Loitxate et al., 2021) to smaller sources that collectively contribute significantly to regional totals (Williams et al., 2025). The complexity is further compounded by considerable temporal variability. Some sources release emissions unpredictably, with emissions turning on and off intermittently, while broader fluctuations occur across production basins due to changing operational conditions (Cusworth et al., 2021, 2022). Therefore, there is considerable variability between inventories for individual countries and regions (Scarpelli et al., 2022), while most studies suggest that CH_4 emissions from the oil and gas industry are underestimated by inventories and agencies (Saunois et al., 2025).

Consequently, CH_4 emission estimates in the EMME region remain highly uncertain, despite the region's substantial contribution to global CH_4 emissions. Reported total emissions for the Middle East vary significantly, ranging from 21 to 47 Tg CH_4 per year (Saunois et al., 2025). Furthermore, the recent release of EDGAR_2025_GHG (Crippa et al., 2025), which incorporates updated energy activity statistics, shows considerable differences in the EMME region compared to its predecessor, EDGAR v8.0 (Crippa et al., 2023). Additionally, also observation-based top-down methods, such as inverse modeling, face

[1] including Bahrain, Cyprus, Egypt, Greece, Iran, Iraq, Israel, Jordan, Kuwait, Lebanon, Oman, State of Palestine, Qatar, Saudi Arabia, Syrian Arab Republic, Turkey, United Arab Emirates (UAE), and Yemen

https://doi.org/10.5194/egusphere-2026-3792
Preprint. Discussion started: 21 July 2026

huge challenges in quantifying emissions in the EMME region due to the scarcity of ground based measurements (e.g. Ricaud et al., 2018; Paris et al., 2021).

Given these limitations, satellite instruments can provide an alternative constraint on CH_4 emissions by detecting atmospheric CH_4 from backscattered sunlight in the shortwave infrared (Jacob et al., 2022). The TROPOspheric Monitoring Instrument (TROPOMI), launched on Sentinel 5P in 2017, has been used in several inversion studies to constrain CH_4 emissions at global (e.g. McNorton et al., 2022) and local (e.g. Shen et al., 2021) scales, as well as to quantify emissions from individual oil and gas basins (e.g. Zhang et al., 2020; Shen et al., 2022). Chen et al. (2023) used TROPOMI observations to quantify CH_4 emissions in the Middle East and North Africa in 2019, revealing significant discrepancies with bottom-up estimates. Their analysis found that total anthropogenic emissions were 35% higher than reported, with emissions from the gas sector exceeding prior estimates by 103%.

Satellite-based inversions predominantly use Eulerian atmospheric transport models to relate total column mole fractions to surface fluxes, employing techniques such as adjoints, Green's functions, or ensemble approaches (Bergamaschi et al., 2009; Varon et al., 2022; Tsuruta et al., 2023). A key advantage of these methods is that their computational cost remains independent of the number of observations, which can be very large when using satellite data. However, Lagrangian particle dispersion models (LPDMs) can offer advantages over Eulerian models by providing more accurate simulations of atmospheric processes like advection and turbulence, allowing to initialize simulations for any given observation geometry and independently of a grid, and ensuring conservation of mass. They also exhibit less numerical diffusion and can simulate both near- and far-field dispersion (Lin, 2012). However, when LPDMs are applied in backward mode, as is common in inverse modeling, the computational cost scales with the number of observations, thereby limiting the number of observations that can be effectively used. Recently, Thompson et al. (2025) developed a methodology for efficiently integrating total column observations into an LPDM-based inversion and applied it in a case study to estimate CH_4 fluxes over Siberia using TROPOMI data. The same methodology was recently adopted by Subramanian et al. (2025) to estimate CH_4 emissions in India.

In this study, we adopt the methodology of Thompson et al. (2025), using TROPOMI observations to estimate CH_4 emissions in the EMME region through an LPDM-based inversion for the year 2020. While improving emission estimates for the EMME region constitutes our primary research objective, we also explore methodological aspects. We employ systematic sensitivity analyses to identify the parameters that most strongly influence inversion results. Similar to Vojta et al. (2025), we explore the relevant parameter space, placing particular emphasis on the baseline optimization. Through these methodological tests, we aim to constrain the inversion setup as robustly as possible in order to derive a reliable and defensible estimate of CH_4 emissions in the EMME region.

https://doi.org/10.5194/egusphere-2026-3792
Preprint. Discussion started: 21 July 2026

2 Methodology

2.1 TROPOMI satellite observations

In this study, we utilize column-averaged CH_4 mole fractions (XCH_4) over the inversion domain[2] (15-65 °E, 10-50 °N), retrieved from TROPOMI data for the year 2020. TROPOMI is an imaging spectrometer aboard the Sentinel-5 Precursor satellite, which follows a polar sun-synchronous orbit. It operates by measuring the solar radiation reflected from Earth's surface using a push-broom technique. The instrument provides near-daily global coverage with a swath width of 2600 km and a nadir ground resolution of 7x5.5 km^2 at approximately 13:30 local overpass time (Veefkind et al., 2012). Retrievals are sensitive to CH_4 at all atmospheric altitudes, including the planetary boundary layer, making them suitable for studying CH_4 emissions (Schneising et al., 2020). We use TROPOMI CH_4 data from the WFM-DOAS (Weighting Function Modified Differential Optical Absorption Spectroscopy) retrieval algorithm, version 1.8 (Schneising et al., 2020, 2023), including only retrievals with a valid quality flag.

To decrease the total number of observations and, consequently, reduce LPDM and inversion computational costs, we aggregate retrievals into so-called "super observations", which also helps to reduce random errors. The level of averaging is determined based on the standard deviation of total column mole fractions, with the spatial resolution adaptively adjusted to retain higher resolution in regions of strong variability (see Thompson et al., 2025). For each day, we apply a two-step averaging process, where we aggregate observations within 0.25° and 0.5° resolution grid cells. Over the course of 2020, the aggregation results in approximately one million super observations entering the inversion. Thompson et al. (2025) and Subramanian et al. (2025) assigned retrievals to the super-observation grid based on their midpoint coordinates, such that retrievals whose ground pixels overlap multiple grid cells are entirely attributed to a single super-observation cell, neglecting their partial contribution to adjacent cells. To better account for such overlaps, we subdivide each retrieval pixel into 25 sub-elements of equal area and assign each sub-element individually to the super-observation grid, calculating an area-weighted averaging of retrieval sub-elements within each grid cell. While this approach provides a more accurate treatment of overlapping ground pixels, we demonstrate in the supplement (Sect. S1) that, for our application, differences compared to the midpoint-based approach remain small (below 0.1%) in most grid cells and reach a few ppb in isolated cells only.

Retrieval errors are likely spatially correlated given that nearby retrievals experience similar atmospheric and surface conditions and are likely influenced by systematic instrumental, algorithmic, or prior-field biases. To account for that, we assume that retrieval errors are correlated within each super-observation cell using a spatial exponential decay function, adopting a correlation length of 30 km based on the findings of Rijsdijk et al. (2025) for NO_2. Finally, derived super observation uncertainties are then used as variances in the observation error covariance matrix.

Super observations in 2020 (Fig. 1a) show highest column mole fractions over Iran, Iraq, and Saudi Arabia, with maxima near the southern Caspian Sea and in regions surrounding the Persian Gulf, where intensive oil and gas production takes place. In contrast, lower mole fractions are observed over Egypt, Libya, and areas north of the Mediterranean Sea. Domain-averaged

[2]Please note that the inversion domain covers the area between 15–65°E and 10–50°N. In contrast, the term EMME region refers to the group of countries within this domain, as defined above, and not to the entire rectangular inversion domain

https://doi.org/10.5194/egusphere-2026-3792
Preprint. Discussion started: 21 July 2026

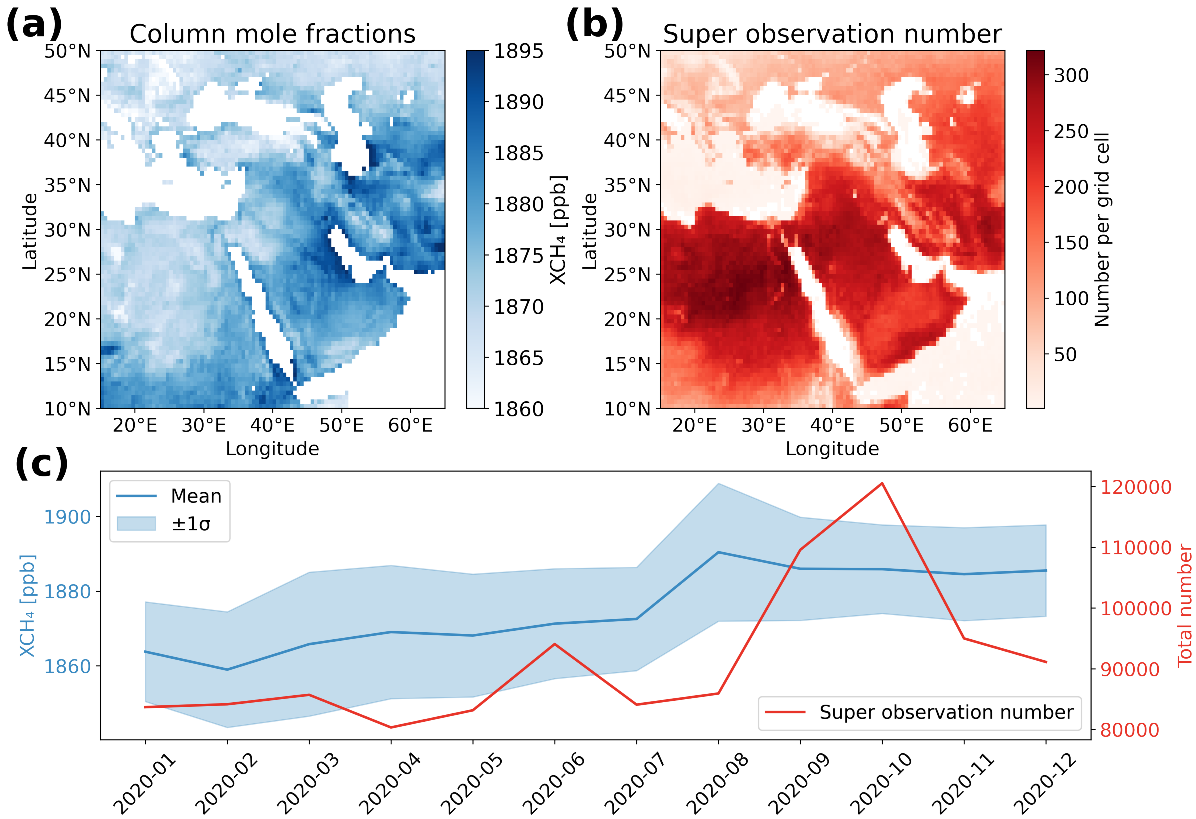

Figure 1. (a) Annually averaged super observation column mole fractions, shown for grid cells with $\geq$ 20 super observations, (b) number of super observations per grid cell; (c) seasonal variation of monthly mean column mole fractions averaged over the entire inversion domain (blue line, with blue shading showing range of one standard deviation) and total number of observations per month within the domain (red line).

column mole fractions (Fig. 1c) show an overall increase throughout 2020, with a pronounced rise between July and August. Notably, this pattern differs from typical time series derived from ground-based in-situ observations, which often exhibit a summer minimum due to enhanced hydroxyl radical (OH) concentrations, although similar seasonality has occasionally been reported also from ground-based stations (e.g. Gialesakis et al., 2023). In contrast, such behavior is not unusual for column measurements (see e.g. Subramanian et al., 2025; Thompson et al., 2025; Kivimäki et al., 2025; Shahzadi et al., 2026) and was primarily attributed to variations in tropopause height (Shahzadi et al., 2026).

Most of the Middle East is well covered by super observations (Fig. 1b), whereas coverage is substantially lower north of the Mediterranean Sea where cloudiness is higher. Coverage over the ocean is very limited, since reliable retrievals are generally restricted to sun-glint conditions. The total number of super observations reaches its maximum in September and October (Fig. 1c).

https://doi.org/10.5194/egusphere-2026-3792
Preprint. Discussion started: 21 July 2026

2.2 A priori emissions

In our inversion, we optimize gridded a priori CH_4 fluxes that comprise contributions from (1) anthropogenic emissions, (2) wetlands, (3) biomass burning, (4) geological sources, (5) termites, (6) rivers and streams, (7) shallow coastal waters and oceans, and (8) soil uptake (sink) fluxes. The datasets used for each source sector were regridded to a common spatial resolution of $0.5° \times 0.5°$ and are listed in Table S1, while the corresponding emissions are illustrated in Fig. S3. Wetlands contribute substantially to total CH_4 emissions in the western Sahel region, while geological emissions are particularly pronounced in Romania due to natural hydrocarbon-related gas seeps (e.g., Baciu et al., 2018). Methane emissions in the EMME region are dominated by anthropogenic sources, which account for approximately 95% of total emissions. For the anthropogenic emissions we use the EDGAR v8.0 dataset (Crippa et al., 2023), which includes contributions from the sectors (i) agriculture, (ii) buildings, (iii) fossil fuel exploitation, (iv) industrial combustion, (v) industrial processes, (vi) power industry, (vii) transport and (viii) waste, as illustrated in Fig. 2. Although agriculture and waste are important contributors, the largest emission fluxes are associated with fossil fuel exploitation, particularly around the Persian Gulf and adjacent coastal regions, with a high density of oil and gas fields. Overall, fossil fuel exploitation accounts for roughly 60% of total CH_4 emissions in the EMME region, as estimated by EDGAR v8.0. A further subdivision of fossil fuel exploitation sector into emissions from gas, oil, and coal is presented in Fig. S4, based on the Global Fuel Exploitation Inventory GFEI v3 (Scarpelli et al., 2025).

A particularly interesting aspect for our study is the recent release of EDGAR_2025_GHG, which shows considerable differences compared to EDGAR v8.0. In the new version, CH_4 emission estimates were updated through revised emission factors for rice cultivation, waste landfilling, and waste incineration, and by including fugitive emissions from abandoned mines (Crippa et al., 2025). However, for the EMME region, we find that the largest differences originate from the fossil fuel exploitation sector. Figure 3 illustrates the differences between the two EDGAR versions for anthropogenic CH_4 emissions in the EMME region, showing the total emissions and the spatial distribution of the differences on a map. EDGAR_2025_GHG shows substantially lower total EMME emissions, largely due to reduced fuel exploitation emissions around the Persian Gulf. Further reductions are found in northwestern Egypt, and western Turkey.

The observed discrepancies in the fuel exploitation sector are most likely related to updated International Energy Agency (IEA) energy statistics, while no major changes in the sectoral emission factor methodologies are explicitly reported by Crippa et al. (2025). For our reference inversions, we use anthropogenic emissions from EDGAR v8.0 as our prior estimate. In addition, we perform inversions using EDGAR_2025_GHG and further construct two additional a priori emission fields by replacing the fuel exploitation sector in both EDGAR inventories with that from the GFEI inventory ("EDGAR v8.0 + GFEI", "EDGAR_2025_GHG + GFEI") to evaluate the robustness of inversion results.

A priori emission uncertainties are specified as a fraction of the corresponding total emission values in each grid cell, implicitly assuming that grid cells with higher emissions also carry proportionally larger uncertainties. For the reference inversion setup, we assume a relative uncertainty of 100% and a minimal value of $1 \cdot 10^{-8}\ \mathrm{kg\,m^{-2}\,h^{-1}}$. In addition, we perform sensitivity tests with uncertainties ranging from 30% to 200%. Spatial and temporal correlations between emission errors are represented using an exponential decay function. In the reference inversions, we assume a spatial correlation length of 100 km

https://doi.org/10.5194/egusphere-2026-3792
Preprint. Discussion started: 21 July 2026

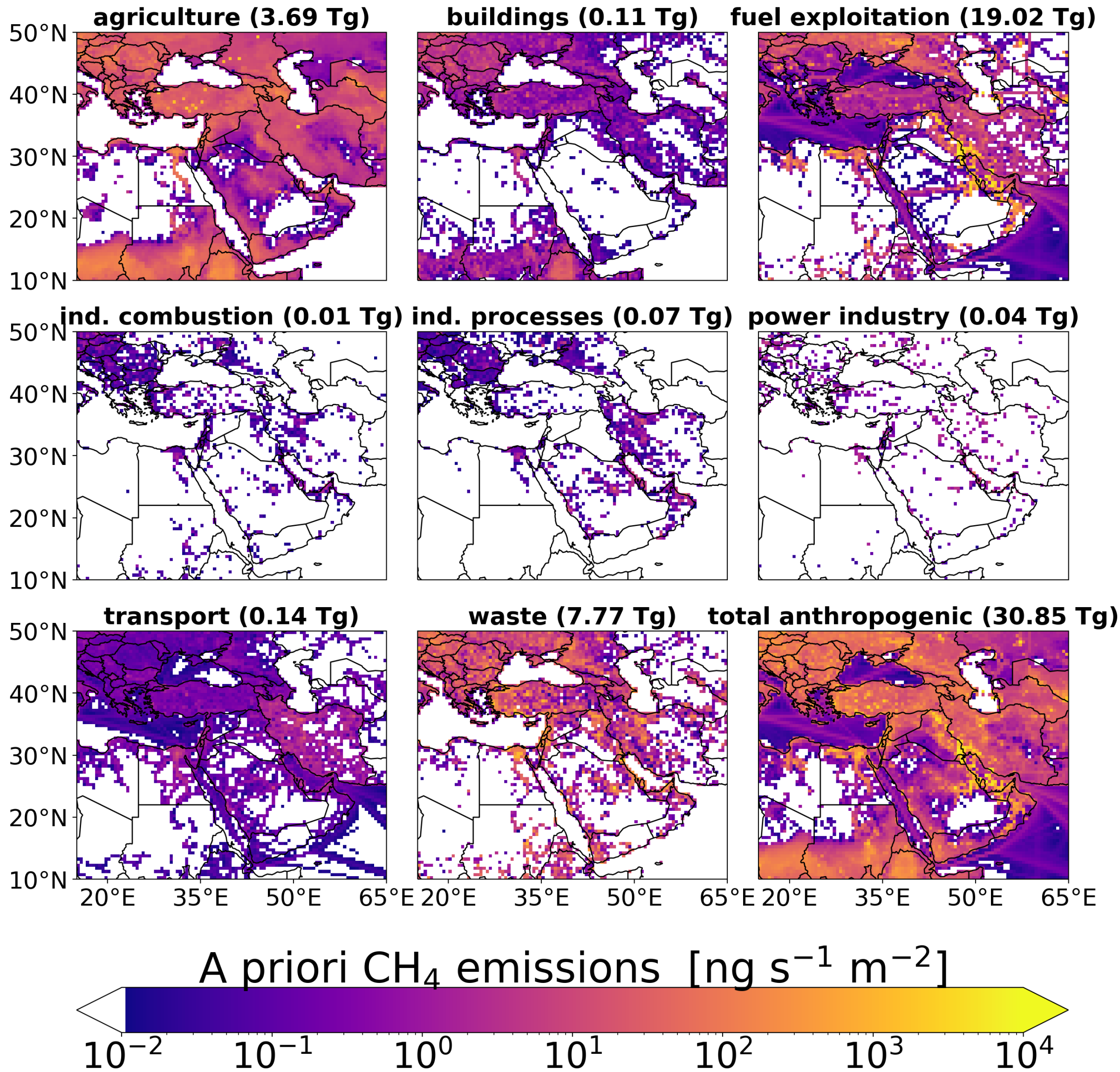

Figure 2. Anthropogenic a priori CH_4 emission from EDGAR v8.0 for the year 2020 including the sectors (i) agriculture, (ii) buildings, (iii) fossil fuel exploitation, (iv) industrial combustion, (v) industrial processes, (vi) power industry, (vii) transport and (viii) waste. The lower right panel shows the sum of all anthropogenic CH_4 emissions. Values in brackets indicate the total 2020 annual emissions for each anthropogenic sector in the EMME region.

and a temporal correlation length of 30 days. Sensitivity tests further explore spatial correlation lengths between 50 and 500 km and temporal correlation lengths between 30 and 180 days.

https://doi.org/10.5194/egusphere-2026-3792
Preprint. Discussion started: 21 July 2026

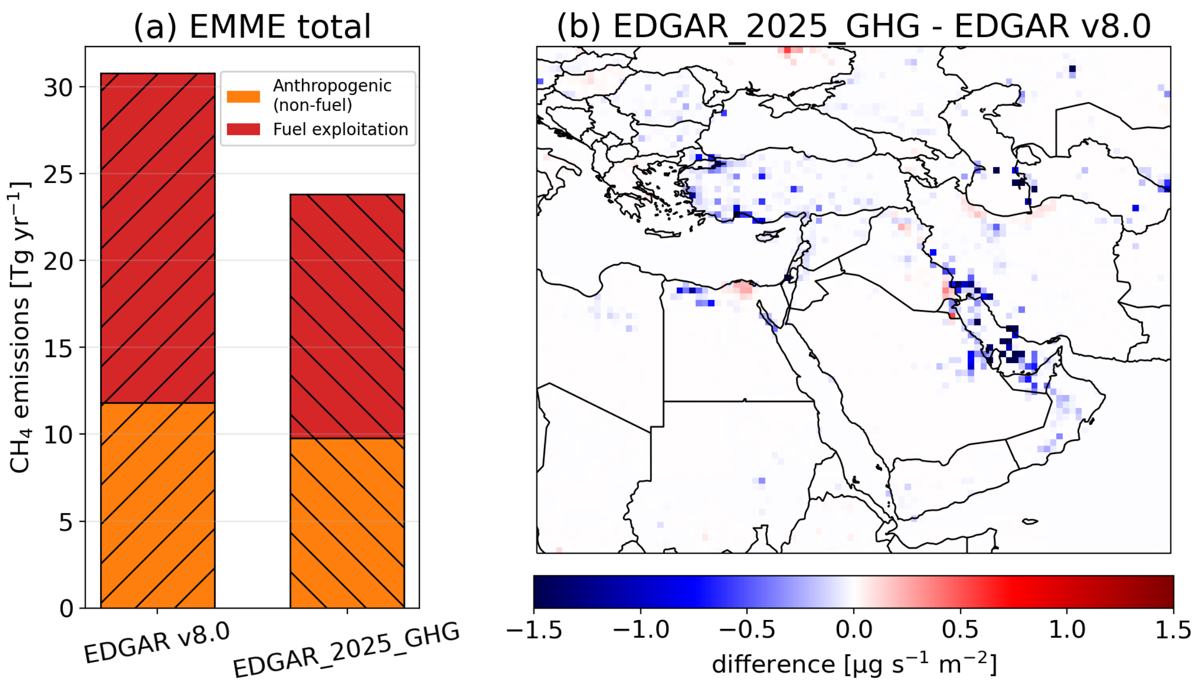

Figure 3. (a) Anthropogenic CH_4 emissions in the EMME region for the year 2020 from EDGAR versions v8.0 and 2025_GHG, showing total emissions with sectoral contributions from fossil fuel exploitation and other anthropogenic sources. (b) Spatial distribution of the differences between both versions.

https://doi.org/10.5194/egusphere-2026-3792
Preprint. Discussion started: 21 July 2026

2.3 Atmospheric transport and modeled mole fractions

A modeled vertical profile of CH_4 mole fractions $\mathbf{x}$ can be compared with the regularized "real" CH_4 profile entering the XCH_4 retrieval by applying the averaging kernel $\mathbf{A}$ used in the retrieval:

$$\mathbf{x}^{\mathrm{m}} = \mathbf{x}^{\mathrm{pri}} + \mathbf{A}\left(\mathbf{x} - \mathbf{x}^{\mathrm{pri}}\right), \tag{1}$$

where $\mathbf{x}^{\mathrm{pri}}$ denotes the a priori profile used in the retrieval, and $\mathbf{x}^{\mathrm{m}}$ represents the model profile corresponding to the regularized retrieval profile (Rodgers and Connor, 2003). For a retrieval defined on N discrete pressure layers, the column-average mole fractions x_{avg} can be expressed as the weighted sum of the contributions from the individual retrieval layers:

$$x_{\mathrm{avg}} = x_{\mathrm{avg}}^{\mathrm{pri}} + \sum_{n=1}^{N} a_n w_n x_n - \sum_{n=1}^{N} a_n w_n x_n^{\mathrm{pri}}, \tag{2}$$

where $x_{\mathrm{avg}}^{\mathrm{pri}}$ represents the prior column-average mole fraction, a_n denotes the n-th element of the column averaging kernel, w_n is a pressure-weighting factor related to the thickness of the corresponding pressure layer, x_n is the modeled mole fraction in a specific layer n, and x_n^{pri} is the prior mole fraction in layer n. To model x_n we use the LPDM FLEXPART 10.4 in backward mode to simulate the atmospheric transport of CH_4, by tracing a large number of virtual particles from the n-th layer to the corresponding surface fluxes for 20 days. When using LPDM models, x_n can be expressed as the sum of two contributions:

$$x_{\mathrm{n}} = \mathbf{H}_n \mathbf{f} + \mathbf{H}_n^{\mathrm{ini}} \mathbf{y}^{\mathrm{ini}} \tag{3}$$

The first term in Eq. 3 represents the contribution from surface fluxes $\mathbf{f}$ occurring within the LPDM simulation period, while the second term corresponds to the contributions from mole fractions present in the atmosphere prior to the simulation period (the so-called baseline), that can be estimated from a 3D field of initial mole fractions $\mathbf{y}^{\mathrm{ini}}$ (see e.g. Thompson and Stohl, 2014). $\mathbf{H}_n$ represents the sensitivity to the fluxes while $\mathbf{H}_n^{\mathrm{ini}}$ represents the sensitivity to the initial mole fractions, both calculated from the LPDM model. Inserting Eq. 3 into Eq. 2 yields:

$$x_{\mathrm{avg}} = x_{\mathrm{avg}}^{\mathrm{pri}} + \sum_{n=1}^{N} a_n w_n \mathbf{H}_n \mathbf{f} + \sum_{n=1}^{N} a_n w_n \mathbf{H}_n^{\mathrm{ini}} \mathbf{y}^{\mathrm{ini}} - \sum_{n=1}^{N} a_n w_n x_n^{\mathrm{pri}}. \tag{4}$$

where the column averaged sensitivities to the fluxes and the initial mole fractions can be expressed as:

$$\mathbf{H}^{\mathrm{col}} = \sum_{n=1}^{N} a_n \mathbf{H}_n w_n, \qquad \mathbf{H}^{\mathrm{col,ini}} = \sum_{n=1}^{N} a_n \mathbf{H}_n^{\mathrm{ini}} w_n. \tag{5}$$

In this formulation, the sensitivities must be computed separately for each retrieval layer and, consequently, requires the maintenance of information about which retrieval layer a particle had originated. Thompson et al. (2025) demonstrated that

https://doi.org/10.5194/egusphere-2026-3792
Preprint. Discussion started: 21 July 2026

the information $a_n w_n$ can be incorporated more efficiently by varying the particle number in each layer, according to $P_n = P\, a_n w_n$, where P denotes the total number of particles released per retrieval. The column averaged sensitivities can then be calculated for a grid cell i, as follows[3]:

$$\mathbf{H}_i^{\mathrm{col}} = \frac{1}{\rho_i}\frac{1}{P}\sum_{p=1} l_{p,i}\,\Delta t_{p,i}, \qquad \mathbf{H}_i^{\mathrm{col,ini}} = \frac{1}{P}\sum_{p=1} l_{p,i}, \tag{6}$$

where ρ_i is the air density in the i-th grid cell, $\Delta t_{p,i}$ is the particle residence time of the particle in the grid cell, and $l_{p,i}$ is a transmission function for the particle p, representing the fraction of particle "mass" remaining, which may change due to atmospheric chemistry. These formulations of the sensitivities produce results consistent with the full layer calculation while requiring substantially less computation time, allowing total column measurements to be treated as efficiently as point observations. The approach is described in detail in Thompson et al. (2025).

In this study, we release 40,000 virtual particles per super observation, and sensitivities are calculated at 0.5° resolution over the inversion domain (15-65 °E, 10-50 °N) and at 2.0° globally[4], both with 30 vertical layers of 0.1, 0.2, 0.35, 0.5, 0.75, 1, 1.5, 2, 2.5, 3, 3.5, 4, 4.5, 5, 6, 7, 8, 9, 10, 12.5, 15, 17.5, 20, 22.5, 25, 30, 35, 40, 45, and 50 km above ground level (agl) interface heights. The flux sensitivities were computed only for the lowest atmospheric layer, extending from 0 to 100 magl, where the majority of emissions occur. To drive the FLEXPART simulations, we use hourly ERA5 wind fields - the fifth generation of the European Centre for Medium-Range Weather Forecasts (ECMWF) atmospheric reanalysis (Hersbach et al., 2018). Specifically, we employ wind fields with a resolution of 0.25°×0.25° for the inversion domain and 0.5°×0.5° for the global domain, each with 137 vertical levels.

2.4 Atmospheric inversion

To estimate CH_4 emissions in the EMME region, we employ the Bayesian inversion framework FLEXINVERT+, which optimizes emissions by minimizing the cost function J:

$$J(\mathbf{z}) = \frac{1}{2}(\mathbf{z}-\mathbf{z}_p)^T\mathbf{B}^{-1}(\mathbf{z}-\mathbf{z}_p) + \frac{1}{2}(\mathbf{H}\mathbf{z}-\mathbf{y})^T\mathbf{R}^{-1}(\mathbf{H}\mathbf{z}-\mathbf{y}), \tag{7}$$

where $\mathbf{y}$ represents the observation vector, $\mathbf{z}$ and $\mathbf{z}_p$ represent the state vector and its a priori values, respectively; $\mathbf{H}$ is the atmospheric transport operator, $\mathbf{R}$ is the observation error covariance matrix, and $\mathbf{B}$ is the a priori error covariance matrix. From a Bayesian perspective, the cost function J is the negative logarithm of the posterior probability distribution, derived through Bayes' theorem (e.g., Tarantola, 2005). Consequently, minimizing J corresponds to maximizing the posterior probability and yields the most probable estimate of emissions (a posteriori emissions). To minimize the cost function, we utilize the M1QN3 algorithm (Gilbert and Lemaréchal, 2006), a quasi-Newton method that approximates the inverse Hessian using limited-memory techniques, making it suitable for large-scale unconstrained minimization problems. After initial tests, we set

[3]The number of terms in the summation depends on the number of particles residing in the ith grid cell

[4]global sensitivities are needed to calculate the baseline

https://doi.org/10.5194/egusphere-2026-3792
Preprint. Discussion started: 21 July 2026

the number of iterations to 20 for the sensitivity experiments, as the cost function showed only minor changes beyond this point. For our final results, however, we increased the number of iterations to 30.

Run-specific uncertainties of the a posteriori emissions are estimated using a Monte Carlo approach (e.g. Tarantola, 2005). An ensemble of 100 inversions is generated by perturbing the a priori emissions according to their prescribed uncertainties. The uncertainty of the resulting a posteriori emissions is then derived from the standard deviation of the posterior emissions across the ensemble.

The state vector is composed of two key components: offsets to the a priori emissions and initial mole fraction scalars. Emission offsets are optimized at a temporal resolution of 30 days and at spatial resolutions of 0.5° or 1.0°, depending on the influence of individual grid cells on the observations (Fig. S5), as determined from emission sensitivities and a priori emissions (Thompson and Stohl, 2014). The baseline is optimized through scaling factors, which adjust the contribution from the initial mole fraction fields aggregated over coarse grid cells. For the initial fields we use the CAMS global greenhouse gas reanalysis EGG4 (Copernicus Atmosphere Monitoring Service, 2021; Agustí-Panareda et al., 2023), and optimize scalars over four latitudinal bands (90°–30°S, 30°S–0°, 0°–30°N, 30°–90°N) and three vertical layers (0–2 km, 2-10 km, and 10–50 km above ground level). Baseline scalars are optimized over 30-day periods, and a relative uncertainty of 1.5% is assumed for the reference inversion. This choice is based on reported monthly errors of approximately 25 ppb in the EGG4 initial fields when compared to surface and tropospheric column observations (Agustí-Panareda et al., 2023). To assess the impact of the uncertainty assigned to the baseline optimization factors, we further test a wide range of values from 0.1% to 7% and investigate the respective inversion results in detail.

The recent version of FLEXINVERT+ provides the option to use a lognormal a priori error distribution. Since fluxes of many species are approximately lognormally distributed (e.g. Cui et al., 2018), their associated uncertainties may also be better represented by a lognormal distribution. This approach is particularly useful when preserving the sign of the fluxes is desired, as it prevents unphysical negative emissions[5]. The cost function for finding the median of the a posteriori distribution reads:

$$J_{\text{med}}(\mathbf{z}) = \frac{1}{2}(\ln(\mathbf{z}) - \ln(\mathbf{z}_p))^\top \mathbf{\Sigma}^{-1}(\ln(\mathbf{z}) - \ln(\mathbf{z}_p)) + \frac{1}{2}(\boldsymbol{H}\mathbf{z} - \mathbf{y})^\top \mathbf{R}^{-1}(\boldsymbol{H}\mathbf{z} - \mathbf{y}) \quad (8)$$

where $\mathbf{\Sigma}$ is the a priori error covariance matrix in log-space, corresponding to uncertainties defined in terms of $\ln(\frac{\mathbf{z}}{\mathbf{z}_p})$. While the recent implementation is described and evaluated in Vojta et al. (2026), further applications are warranted to assess its performance. Therefore, we apply this approach in addition to using a normal a priori distribution to test the robustness of our inversion results.

2.5 Sensitivity tests

We perform a series of sensitivity tests to investigate key challenges and parameter dependencies when using satellite data in atmospheric inversions. We put a focus on the baseline optimization, motivated by the studies of Thompson et al. (2025) and Subramanian et al. (2025), whose approach we follow and who employed the same baseline optimization methodology.

[5] notice that the soil sink of CH_4 is rather small and should rarely lead to net negative fluxes

https://doi.org/10.5194/egusphere-2026-3792
Preprint. Discussion started: 21 July 2026

Both studies used the 2020 EGG4 initial mole-fraction fields but assumed substantially different uncertainties for the baseline scaling factors. Subramanian et al. (2025) applied uncertainties between 0.3% and 0.7%, derived from RMSD differences between EGG4 and TROPOMI datasets, whereas Thompson et al. (2025) adopted a much larger uncertainty of 5% to compensate for substantial baseline biases. While this larger uncertainty allowed biases in the initial mole-fraction fields to be well corrected, a posteriori emissions remained relatively close to the a priori values. This may indicate that a substantial share of the observational information was accommodated by the baseline optimization, particularly in the context of relatively limited observational coverage over their study region, Siberia. This behavior motivates the systematic investigation presented here. Similar to Vojta et al. (2025), we systematically explore the parameter space, starting from a reference inversion setup. We test:

- baseline uncertainties of 0.1, 0.3, 0.5, 0.7, 1.0, 1.3, 1.5, 2.0, 2.5, 3.5, 5, and 7%.
- four different a priori emission data sets: (i) EDGAR v8.0, (ii) EDGAR_2025_GHG, (iii) EDGAR v8.0 + GFEI, (iv) EDGAR_2025_GHG + GFEI (see Sec. 2.2)
- a priori emission errors of 30, 50, 100, 150, and 200%.
- spatial error correlation lengths of 50, 100, 175, 250 and 500 km.
- temporal error correlation lengths of 30, 90 and 180 days.
- a lognormal a priori error distribution in addition to the normal distribution.

3 Results and discussion

3.1 Observed and modeled column mole fractions

Figure 4 shows the daily means of observed column mole fractions averaged over the inversion domain, together with the corresponding averages of the a priori and a posteriori modeled mole fractions and their respective contributions from the baseline. While the a priori modeled mole fractions exhibit large discrepancies compared to the observations, the inversion brings the a posteriori mole fractions much closer to the observed values, confirming the proper functioning of the optimization process with respect to the second term in the cost function. The large discrepancies in the a priori modeled mole fractions originate most likely from a bias in the initial mole fraction fields, leading to a baseline that even exceeds the observations during some periods of the first half of the year, indicating that the EGG4 initial mole fraction fields are too high. Indeed, Agustí-Panareda et al. (2023) reported a relatively strong EGG4 positive bias in the upper troposphere–lower stratosphere, a region strongly influenced by long-range transport and characterized by large uncertainties in CH_4 chemical loss. They also noted that the assimilated satellite data were not able to effectively constrain stratospheric CH_4 in their reanalysis, which likely explains the positive baseline bias observed here.

The inversion is able to correct this bias, as reflected in the a posteriori baseline, which is shifted toward lower values by approximately 20 ppb during this period. A similar seasonal pattern in the baseline optimization was reported by Thompson

https://doi.org/10.5194/egusphere-2026-3792
Preprint. Discussion started: 21 July 2026

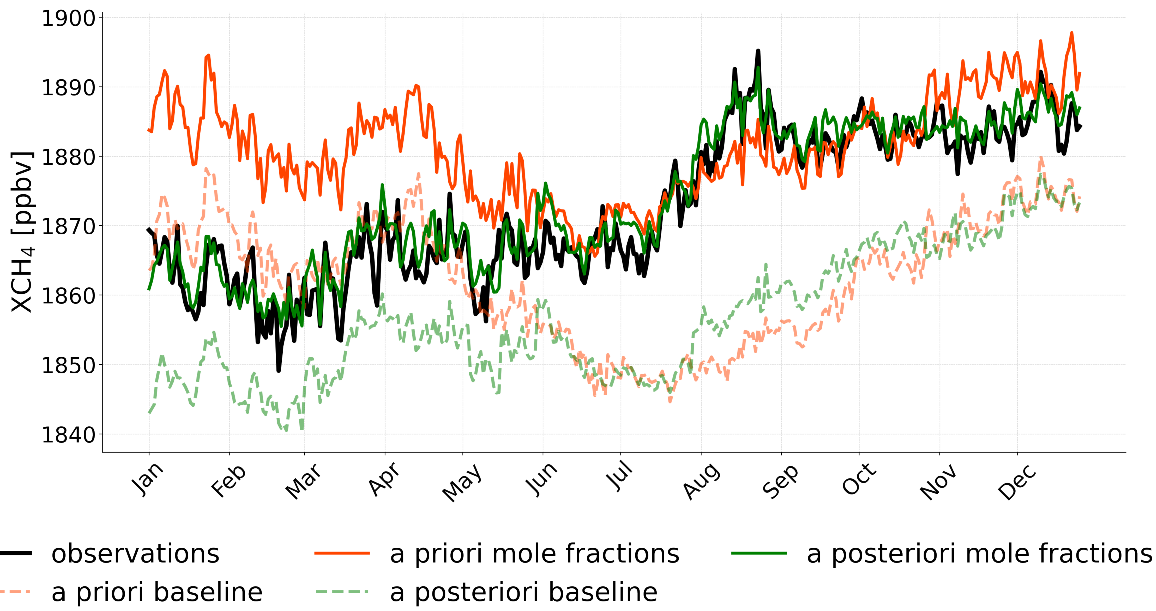

Figure 4. Daily averages of observed column mole fractions (solid black line), a priori modeled column mole fractions (solid red line), a posteriori modeled column mole fractions (solid green line), the a priori baseline (dashed red line), and a posteriori baseline (dashed green line), averaged over the study domain.

et al. (2025), likewise suggesting that the EGG4 fields may be biased during early 2020. However, the baseline corrections needed in our inversion are only about half as large as theirs. An additional validation against an independent dataset from the TCCON station in Nicosia is provided in the supplementary section S4. Notice, that the observations at Nicosia show a similar seasonal pattern than the domain averaged observed mole fractions shown in Fig. 1 and Fig. 4.

3.2 Spatial analysis of inversion results

Figure 5 shows (a) the inversion increments (a posteriori minus a priori emissions), (b) the relative error reduction, calculated for each grid cell based on the a priori and a posteriori Monte Carlo ensemble (see Sect. 2.4), (c) the a posteriori emission distribution, and (d) the a posteriori ensemble emission uncertainty. The results in Fig. 5a,c are shown for the reference inversion, averaged over the year 2020. The inversion produces the largest emission corrections in regions surrounding the Persian Gulf, where a posteriori emissions are substantially reduced compared to the prior estimates. Strong negative increments are also found in northern Iraq and the Baku region, while positive increments occur in eastern Saudi Arabia. All of these adjustments are associated with substantial error reductions, consistent with the good observational coverage in these areas, particularly around the Persian Gulf (see Fig. 1). Sensitivity tests show that these increments persist across all tested configurations, as discussed in detail in Appendices A-F. Taken together, these features suggest robust emission adjustments in those regions.

https://doi.org/10.5194/egusphere-2026-3792
Preprint. Discussion started: 21 July 2026

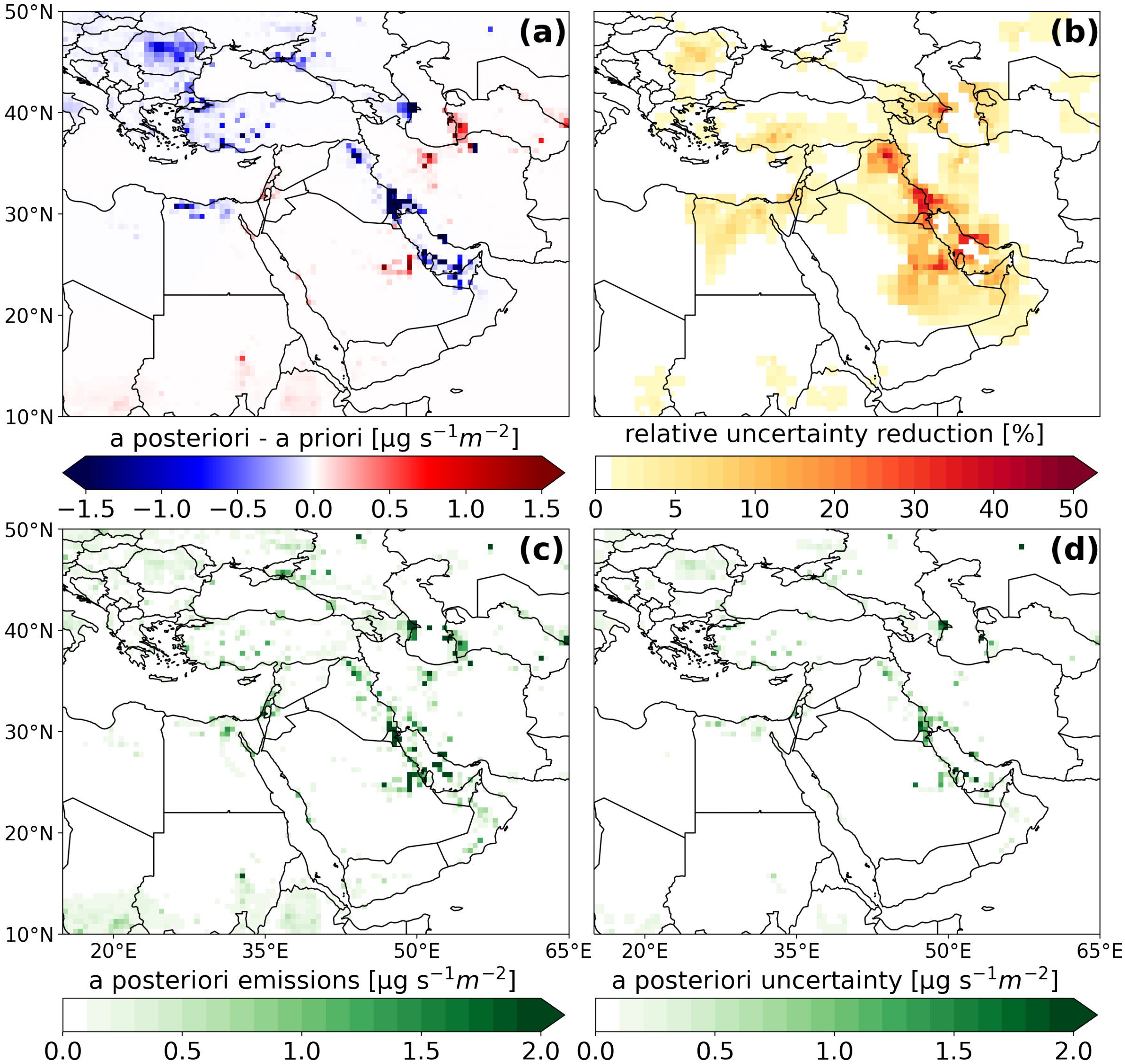

Figure 5. Results of the reference inversion. (a) Emission increments from the inversion (a posteriori–a priori emissions), (b) relative error reduction, (c) a posteriori emission distribution, and (d) a posteriori uncertainty obtained for our reference inversion and averaged over the year 2020.

Figure 5a also shows pronounced negative increments over Romania, western Turkey, northern Egypt, and regions northwest of the Black Sea, while positive adjustments are found in Iran and Turkmenistan. However, the corresponding grid cells exhibit much smaller relative error reductions. Particularly for regions north of the Mediterranean Sea, this can be attributed to substantially worse observational coverage caused by more extensive cloud cover (see Fig. 1). Romania, for example, shows

https://doi.org/10.5194/egusphere-2026-3792
Preprint. Discussion started: 21 July 2026

strong negative increments but only limited error reduction, indicating that the results are less robust than in the Persian Gulf region. This is further reflected in relatively large posterior emission uncertainties (Fig. 5d) compared to the magnitude of the optimized emissions (Fig. 5c), as well as in the larger spread of results across our sensitivity experiments (Appendices A-F).

Our inversion increments show many similarities to the updates from EDGAR v8.0 to EDGAR_2025_GHG (see Fig. 3), with both datasets exhibiting strong negative adjustments in regions surrounding the Persian Gulf. Consistent negative adjustments are also found in north-western Egypt and western Turkey. However, as discussed above, the inversion-derived increments appear less robust in this region.

3.3 Sensitivity analysis results

The results of our sensitivity tests are presented in detail in the Appendices A-F; here we summarize the most important findings.

- The baseline uncertainty emerges as an important inversion parameter: it must be large enough to correct biases in the initial mole fraction fields, but if set too high, the baseline optimization will artificially compensate for emission adjustments, reducing the magnitude of the inversion increments. By examining how the optimization factors evolve with increasing uncertainty, we identified a transition range where bias correction is effective and posterior emissions are robust. Changes in a priori emission errors or their correlations alter the balance between adjustments to emissions and the baseline, shifting this transition range. Consequently, overly large a priori emission errors or strongly correlated errors can introduce biases similar to those caused by too small baseline uncertainties, and vice versa.

- Despite large differences in the a priori inventories, inversion results show remarkably robust posterior emissions for the total emissions in the EMME region and major emitting countries, with the exception of Saudi Arabia, where all inversions indicate significant upward corrections but differences between the posterior emissions are of almost the same magnitude as the differences from the prior emissions (see Fig. 6).

- Inversion patterns are largely similar whether a lognormal or normal a priori error distribution is used, but downward corrections are in some cases less pronounced with the lognormal choice.

- Despite substantial variation in the error assumptions, all tested inversion configurations show persistent negative increments around the Persian Gulf.

Based on our sensitivity tests, we chose the a priori state vector uncertainties used in the reference inversion (baseline uncertainty of 1.5%, a priori fractional emission uncertainty of 100% with a spatial correlation of 100 km and a temporal correlation of 30 days), as they correspond to a stable range of posterior emissions where biases in the initial conditions seem to be largely corrected while coherent emission increment patterns are preserved. For total EMME emissions and for major emitting countries such as Iran and Iraq, the inversion results are generally robust to the choice of a priori inventory and error distribution. However, for some other countries, posterior emissions exhibit greater variability across these choices (Fig. S7), indicating larger uncertainties than estimated by the Monte Carlo ensembles (see Sect. 2.4). The opposite is true if inventories

https://doi.org/10.5194/egusphere-2026-3792
Preprint. Discussion started: 21 July 2026

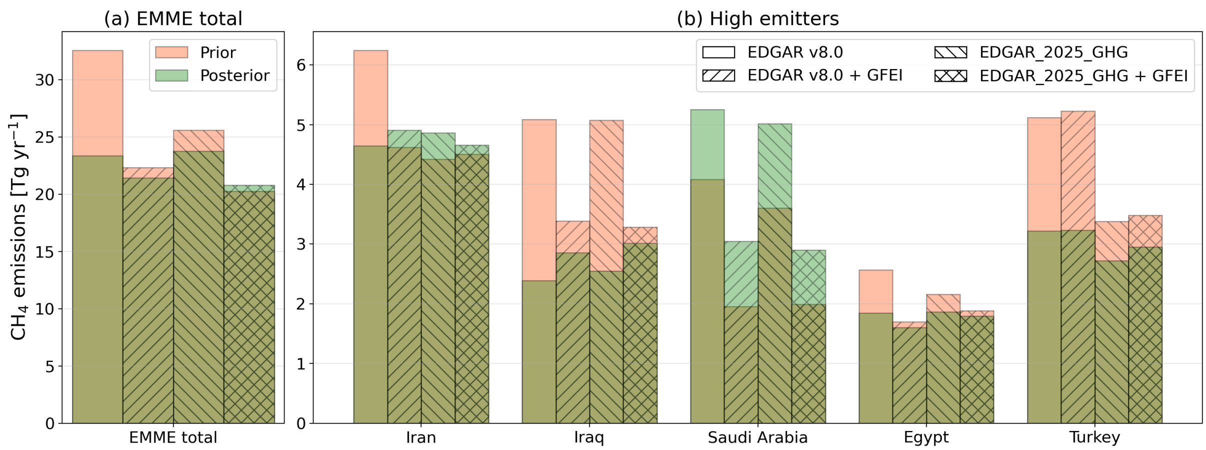

Figure 6. A priori (red) and a posteriori (green) emissions from inversions using different a priori inventories are shown for the EMME region as a whole, as well as for Iran, Iraq, Saudi Arabia, Egypt, and Turkey. The a priori and a posteriori bars are overlaid: red segments indicate downward corrections, while light green segments indicate upward corrections relative to the a priori emissions.

are similar for regions with sparse observational coverage and small a priori emissions, where a posteriori results tend to remain close to the a priori values. In these cases, the ensemble-based uncertainties are larger, likely providing a more realistic estimate of the true uncertainty. To provide the most representative results, we define our final emissions as the average across eight inversion cases, combining the four a priori inventories with the two error distribution choices, while for each country, the associated emission uncertainty combines both the 1σ uncertainties from the Monte Carlo ensemble for each of the eight cases (σ_i) and the 1σ spread over the eight inversion results (σ_{spread}) as:

$$\sigma = \sqrt{\frac{1}{8}\sum_{i=1}^{8}\sigma_i^2 + \sigma_{spread}^2} \qquad (9)$$

3.4 National emissions

Figure 7 and Table S2 show the total CH_4 a posteriori emissions in the EMME region, as well as the national emissions of all countries in this region, while Fig. S7 shows the results for the individual runs, combining the four a priori inventories with the two error distribution choices. We estimate total EMME emissions of 22.4 ($\pm$1.9) Tg yr^{-1}, which is substantially lower than estimated by the EDGAR v8.0 inventory and much closer to those from EDGAR_2025_GHG and the GFEI dataset. Together with the robust inversion increments around the Persian Gulf that are similar to the difference between the EDGAR_2025_GHG and EDGAR v8.0 emissions in this region, this suggests that updates in the newer inventory versions have led to substantial improvements, largely consistent with our inversion results.

We compare our national a posteriori emissions to top down estimates from Chen et al. (2023), Worden et al. (2022), and Western et al. (2021), as well as to national reports submitted to the United Nations Framework Convention on Climate Change

https://doi.org/10.5194/egusphere-2026-3792
Preprint. Discussion started: 21 July 2026

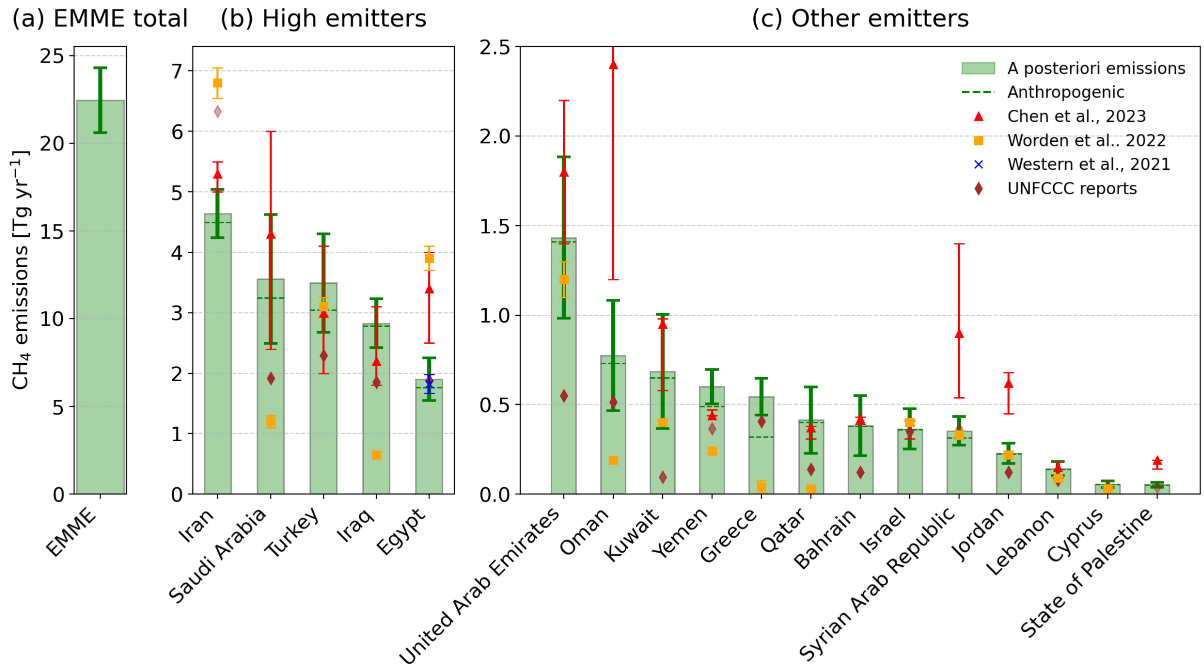

Figure 7. Inversion results showing the a posteriori emissions for (a) the entire EMME region, (b) high-emitting countries, and (c) other EMME countries. Green bars indicate total regional and national emissions, while the error bars represent the 1-σ uncertainty as defined in Eq. 9. The dashed green horizontal lines denote the anthropogenic emission contribution, based on prior sectoral fractions, to facilitate comparison with literature values. Red triangles show anthropogenic CH_4 emissions from Chen et al. (2023) for 2019, yellow rectangles from Worden et al. (2022) for 2019, and the blue cross the total 2017 emissions for Egypt from Western et al. (2021). Brown diamonds represent national reports to UNFCCC, listed in Table S3, with less recent reports displayed with transparent symbols.

(UNFCCC), which (apart from Greece) are provided on a voluntary basis and at irregular intervals. Chen et al. (2023) reported anthropogenic emissions for the Middle East and North Africa for the year 2019 using TROPOMI satellite observations in an analytical inversion based on the GEOS-Chem chemical transport model, in which emissions were optimized over a state vector of approximately 600 elements and subsequently mapped onto a finer 0.25° × 0.3125° grid. Worden et al. (2022) used GOSAT total column CH_4 observations and the GEOS-Chem model to estimate a top-down 2019 anthropogenic CH_4 budget, optimizing emissions on a global 2° × 2.5° grid. Western et al. (2021) estimated total CH_4 emissions for North African countries, including Egypt, using GOSAT observations and the Lagrangian particle dispersion model NAME within a hierarchical Bayesian inversion framework, with results reported up to 2017.

For the high-emitting countries, our results are in good agreement with Chen et al. (2023), except for Egypt, for which our inversion shows a downward correction, in contrast to the large positive increments reported in their study. However, our estimated Egyptian emissions of 1.9 (±0.4) Tg yr^{-1} are almost identical to those reported by Western et al. (2021) for 2017, and are also consistent with the 2020 value submitted by Egypt in its first Biennial Transparency Report to UNFCCC.

https://doi.org/10.5194/egusphere-2026-3792
Preprint. Discussion started: 21 July 2026

For Iran, we obtain an emission of 4.6 (±0.4) Tg yr^{-1}, indicating a clear downward correction relative to the EDGAR v8.0 inventory. Our estimate is substantially lower than the value reported for 2010 in Iran's Third National Communication to UNFCCC, which may also explain the comparatively high emissions in EDGAR v8.0 Oil production in Iran has been substantially reduced in recent years due to sanctions, likely contributing to smaller emissions. For Iraq, we likewise find consistent downward corrections across all tested cases, yielding an a posteriori emission estimate of 2.8 (±0.4) Tg yr^{-1}, which nevertheless remains higher than the 2019 value reported to UNFCCC in the Second National Communication and First Biennial Update Report. For Iran and Iraq, our results are robust across all sensitivity tests, leading to comparatively narrow uncertainty intervals, which is consistent with the substantial reduction in emission errors in this region. For both countries our 2020 estimates are similar to the 2019 emissions reported by Chen et al. (2023), despite the large changes to the EDGAR v8.0 inventory.

For Turkey, our estimate of 3.5 (±0.8) Tg yr^{-1} is also in good agreement with Chen et al. (2023) and exceeds the 2020 value reported in the Eighth National Communication and Fifth Biennial Report. Notably, a posteriori uncertainties are larger than for Iran and Iraq. While robust downward corrections are obtained when assuming a normal a priori distribution, these corrections are smaller when using a lognormal prior, resulting in larger uncertainties. Other sensitivity tests also show greater variability, consistent with a smaller reduction in errors in this region.

For Saudi Arabia, our estimate of 3.6 (±1.1) Tg yr^{-1} is likewise close to that of Chen et al. (2023) and considerably higher than the reported 2019 value. However, similar to their study, uncertainties remain relatively large, as posterior emissions are more sensitive to changes in the inversion settings.

For the smaller emitters in the EMME region, our results are generally in good agreement with Chen et al. (2023) for UAE, Kuwait, Yemen, Qatar, Bahrain, and Lebanon, whereas our estimates are substantially lower for Oman, Syria, Jordan, and Palestine. However, the very large uncertainties reported by Chen et al. (2023) for Oman and Syria highlight that emissions in these regions remain poorly constrained. In general, for many of these low-emission countries (including Cyprus, Israel, Jordan, Lebanon, Oman, Palestine, Syria, and Yemen) only minor corrections are introduced by the inversion, such that the posterior emissions largely reflect the prior inventories. More pronounced and relatively robust corrections are found for Bahrain and Qatar, for which we also obtain the best agreement with Chen et al. (2023).

For many of the major oil and gas producing countries discussed (Iran, Saudi Arabia, UAE, Oman, and Kuwait), the 2019 emissions reported by Chen et al. (2023) are either higher than, or at the upper end of the uncertainty range of our estimates. These systematic differences may be explained by reduced oil production in 2020 following the COVID-19 demand collapse, as further discussed in the next section.

On average, national emissions reported to UNFCCC are about half as large as our inversion-based estimates (unweighted mean), corresponding to a regional difference of 29% when weighted by emissions, reflecting the substantially larger relative discrepancies for smaller emitters. In addition to Iran, Greece also represents an exception, which is the only Annex I country in the region required to report its emissions annually. Here, our inversion suggests modest but relatively consistent downward corrections, yielding total national emissions of about 0.55 ± 0.10 Tg yr^{-1}. Given the larger contribution of natural sources in

https://doi.org/10.5194/egusphere-2026-3792
Preprint. Discussion started: 21 July 2026

Greece compared to other EMME countries, our estimated anthropogenic emissions of 0.35 Tg yr^{-1}, based on prior sectoral fractions, are relatively close (~13% lower) to the reported value.

Except for the smallest emitters, for which our results closely follow the prior inventories, we find relatively poor agreement with Worden et al. (2022). This may partly reflect their coarse global inversion grid (2° × 2.5°), which likely limits the ability to distinguish emissions from neighboring countries with proximate sources, such as in the Persian Gulf region, and may lead to a reduced representation of smaller countries. In addition, the global inversion may be relatively weakly constrained in some regions due to the sparser spatial coverage of GOSAT observations.

To assess the extent to which posterior national CH_4 emissions from the fuel exploitation sector scale with oil and gas production in the EMME region, we apply a regression analysis, between posterior emissions and national production data, which is explained in detail in the supplementary section S7. The regression shows limited explanatory power, suggesting that a simplified representation based on uniform emission factors, as commonly used in bottom-up inventories, cannot capture the variability in emissions across EMME countries. We observe clear country-specific deviations from the regression fit, broadly consistent with heterogeneous emission intensities from Chen et al. (2023), suggesting that factors beyond production (such as infrastructure, operational practices, and mitigation measures) play an important role.

3.5 Emission decline over 2020

The economy was heavily impacted by the COVID-19 pandemic in 2020. As a consequence of global lockdowns, mobility, which accounts for approximately 57% of global oil demand, declined substantially, with global road transport activity dropping to about 50% of 2019 levels by the end of March 2020. Accordingly, oil demand decreased drastically (see Fig. S8), reaching a minimum in April and May at up to 29 million barrels per day (Mb d^{-1}) below 2019 levels, corresponding to demand levels last seen in 1995 (IEA, 2020).

As a result, major oil-producing countries such as Iran were forced to significantly reduce crude oil production, with Iran's output reaching the lowest levels in four decades as storage capacity approached its limits due to reduced exports and refinery throughput (Al Jazeera, 2020). To investigate whether these production cuts affected CH_4 emissions, we first examine the monthly emission time series for Iran (Fig. 8a), where our annual a posteriori emissions are robust. Our results suggest a pronounced minimum in May, coinciding with the collapse in global oil demand and the decrease in monthly oil production (see Fig. S8 and S9). However, oil production remained low in summer, while a posteriori emissions started to increase after May, which might reflect a gradual increase of exports after May (Rosenberg and Nada, 2022). In addition, regional analyses have shown a pronounced seasonal cycle in atmospheric CH_4 over Iran, with a late-summer maximum that has been attributed to enhanced emissions from wetlands and agricultural sources (Mousavi et al., 2024). Note, that a similar pattern in CH_4 emissions has been reported for the Permian Basin in the United States, where emissions were strongly correlated with declining oil prices during the same period (Lyon et al., 2021).

Following the demand collapse, OPEC+ (Organization of the Petroleum Exporting Countries) implemented historically large crude oil production cuts of approximately 9.7 Mb d^{-1} starting in May 2020, which were later partially relaxed to 7.7 Mb d^{-1} but remained in effect until the end of the year (IEA, 2020). Consequently, crude oil production in major OPEC+ producers

https://doi.org/10.5194/egusphere-2026-3792
Preprint. Discussion started: 21 July 2026

such as Saudi Arabia, Iraq, UAE, and Kuwait dropped sharply in mid-2020 and remained substantially lower in the second half of the year compared to pre-pandemic levels (TradingEconomics.com, 2026). Our corresponding emission time series for Saudi Arabia (Fig. 8b), Iraq, UAE, and Kuwait (Fig. S10) show a rather persistent decline throughout 2020. While our individual timeseries do not strictly follow the exact production pattern (sharp drop in May), they might still suggest that production cuts have contributed to reduced CH_4 emissions.

The total emissions for the EMME region (Fig. 8c) also show an overall decrease during the course of 2020, interrupted by a summer peak, which is largely driven by the emissions in Iran. While the overall decrease is consistent with reduced oil activity during the COVID-19 pandemic, we believe that the apparent seasonal signal should be interpreted with caution, as it may also partly reflect potential methodological biases. Based on our sensitivity tests, biases in the initial CH_4 fields are our main concern, as they can strongly influence the apparent seasonal cycle. Although Fig. 4 shows that baseline biases can generally be corrected, residual biases likely vary with season and altitude and may still contribute to variations that could be mistakenly attributed to emission changes. One example is the outflow of the Asian summer monsoon, which delivers CH_4 emissions from South Asia at high altitudes to the EMME region that may not be well captured in our initial CH_4 concentration fields (e.g. Lelieveld et al., 2002). The seasonal signal is particularly sensitive to assumed baseline uncertainties (Fig. S11), making the results less certain, particularly the relatively pronounced decline toward the end of the year when observational coverage also decreases. Consistent with this, sensitivity tests further show that assuming a lognormal error distribution produces a weaker decline in late 2020 compared to a normal distribution (Fig. S25). Overall, longer time series would be required to confirm the inferred declining trends. However, industry-based satellite analyses (Kayrros, 2022) report a substantial reduction in CH_4 super-emitter events (with emission rates on the order of 5–25 t h^{-1} or higher) for many major OPEC+ producers. In Iraq, for instance, such events decreased from 15 events in 2019 to only 4 in 2020, along with reduced emission intensities, which could have led to the pronounced reductions observed in our study.

4 Conclusion

In this study, we investigated CH_4 emissions for the year 2020 in the EMME region using an atmospheric inversion, based on TROPOMI satellite observations. Our main findings are the following:

- Our inversions show robust downward corrections of emissions in the costal areas of the Persian Gulf compared to the EDGAR v8.0 inventory used as a priori information, leading to total EMME emissions of 22.4 ($\pm$1.9) Tg yr^{-1}. Similar reductions are found in the recently updated EDGAR_2025_GHG data set, suggesting that updates to energy activity data in the newer inventory version have led to substantial improvements, broadly consistent with our satellite observation-constrained inversion results. This provides an interesting example in which independent refinements from a top-down approach converge with updates from a bottom-up inventory, illustrating how observational constraints and inventory development can jointly improve our understanding of regional emissions.

https://doi.org/10.5194/egusphere-2026-3792
Preprint. Discussion started: 21 July 2026

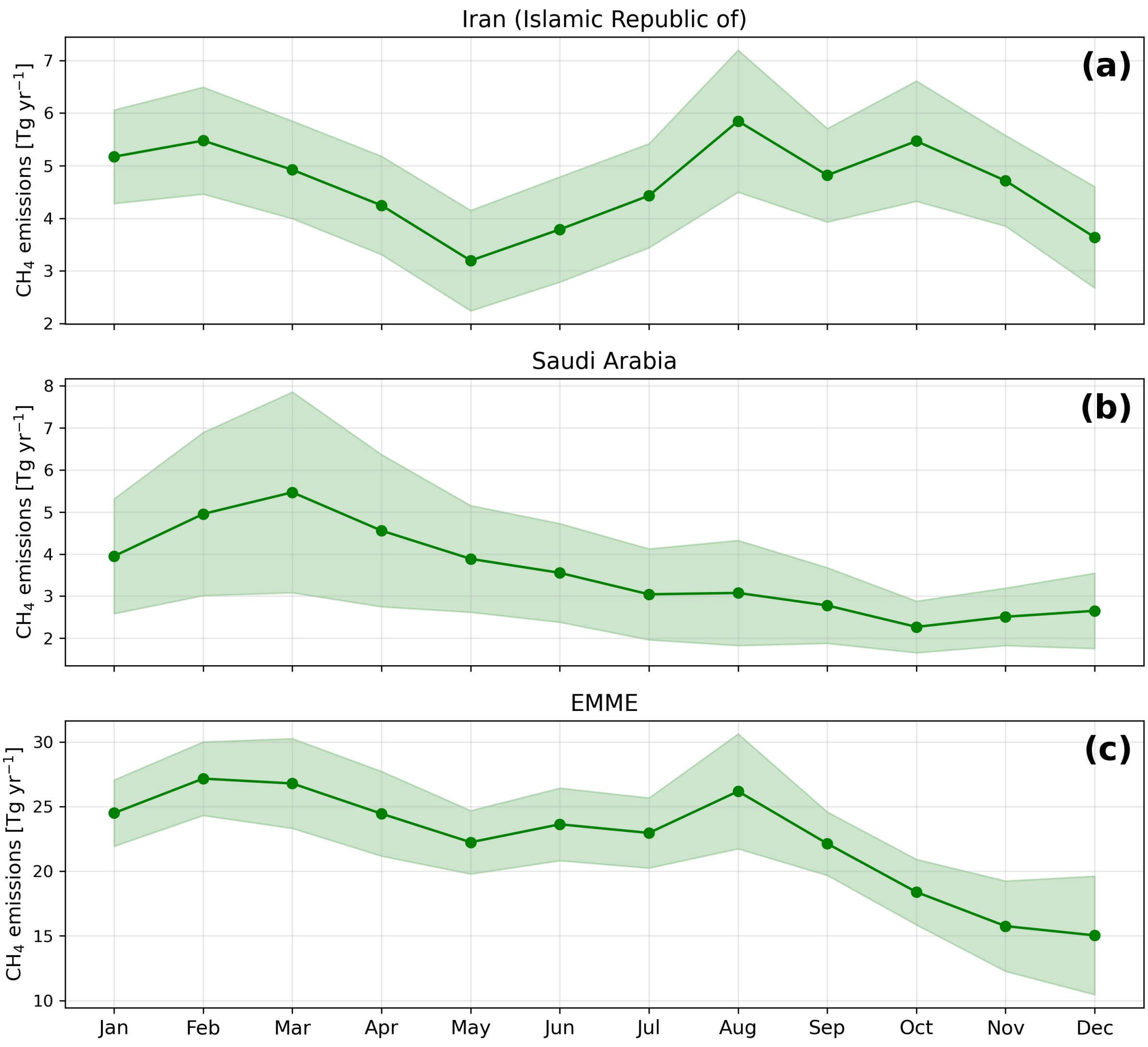

Figure 8. Time series of monthly a posteriori emissions over the year 2020 for (a) Iran, (b) Saudi Arabia, and (c) the total emissions in the EMME region.

https://doi.org/10.5194/egusphere-2026-3792
Preprint. Discussion started: 21 July 2026

- Our inversion yields national emissions of 4.6 (±0.4), 3.6 (±1.1), 3.5 (±0.8), 2.8 (±0.4), and 1.9 (±0.4) Tg yr^{-1} for the high emitting countries Iran, Saudi Arabia, Turkey, Iraq, and Egypt, respectively. While our estimate for Iran is lower than the value reported for 2010 in Iran's Third National Communication to the UNFCCC, this is consistent with reduced oil production due to international sanctions in recent years. In contrast, our inversions indicate higher emissions for Saudi Arabia, Turkey, and Iraq compared to their voluntary national reports (for 2019, 2020, and 2019, respectively), whereas the estimate for Egypt is in very good agreement with the reported 2020 emissions.

- Our results are in good agreement with the TROPOMI-based inversion study of Chen et al. (2023), but show poor agreement with the GOSAT-based study of Worden et al. (2022), both of which use the GEOS-Chem model. This may suggest that the improved observational coverage of TROPOMI can enhance inversion performance and lead to more consistent emission estimates, in addition to the higher inversion resolution used in our study compared to Worden et al. (2022).

- While we find that many countries in the EMME region strongly underestimate their emissions, the emissions reported by Greece — the only country in the region required to submit annual emissions inventories to the UNFCCC — shows good agreement with our results, slightly exceeding our inversion estimate. This may suggest that mandatory reporting frameworks can contribute to more complete and potentially more robust emission estimates.

- Our regression analysis indicates that gross national oil and gas production alone cannot explain the variability in fuel-sector methane emissions across EMME countries. Different country-specific emission intensities affect the methane emissions.

- Our inversion results for the EMME region indicate an overall decrease in emissions during 2020, consistent with oil production reductions during the COVID-19 pandemic. In particular, Iran shows a pronounced emission minimum in May, coinciding with the collapse in global oil demand. Other major emitters, such as Saudi Arabia, Iraq, UAE, and Kuwait, exhibit a sustained decrease throughout the year, suggesting that large-scale OPEC+ production cuts could have led to smaller emissions. While, together, these results suggest that reduced oil activity during 2020 could have led to a measurable decrease in regional CH_4 emissions, the seasonal variations in monthly emissions are more uncertain and should be interpreted with caution, as they may be affected by residual biases in the initial mole fraction fields.

- The use of satellite observations for atmospheric inversions has increased in recent years, driven by improved data quality and availability in regions with limited ground-based monitoring. The robustness of satellite-based inversions, however, still remains an active area of research. Overall, our results suggest that satellite observations can provide strong constraints and substantially reduce a priori biases in regions with large emission signals and good observational coverage (e.g. Iran, Iraq). However, other regions show greater sensitivity to uncertainty settings and a priori estimates. We therefore highlight the importance of sensitivity tests, which help to assess the robustness and accuracy of the results beyond formal uncertainty reduction.

- We find that baseline uncertainty can be an important inversion parameter when substantial biases exist in the initial mole fraction fields, as it controls the balance between correcting these biases and adjusting emissions. We identify a transition range in which bias correction is effective and posterior emissions remain stable. This transition range also depends on the choice of a priori emission errors and their correlations, which similarly influence the balance between baseline and emission adjustments and can therefore be indirectly linked to the baseline optimization. We suggest that inversions could benefit from a more sophisticated representation of baseline uncertainties, for example by allowing scalar uncertainties to vary regionally. This may be particularly beneficial in the presence of known initial field biases, such as the overestimation in the upper troposphere–lower stratosphere in the EGG4 product.

- We emphasize that particular effort should be devoted to obtaining accurate initial mole fraction fields and realistic estimates of their uncertainties, which could substantially improve inversion results based on satellite observations. In the context of the discussed robustness of satellite-based inversions, improved initial fields and baseline optimization may also enhance inversion performance in regions with less observational coverage or weaker emission signals, and could help to derive a more robust seasonal pattern.

Acknowledgements. The development of the TROPOMI/WFMD product received funding from the European Space Agency (ESA) via the projects GHG-CCI+ and MethaneCAMP (ESA contract nos. 4000126450/19/I-NB and 4000137895/22/I-AG) and from the Federal Ministry of Research, Technology and Space (BMFTR) within its project ITMS via grant no. 01 LK2103A. The TROPOMI/WFMD retrievals were performed on HPC facilities of the IUP, University of Bremen, funded under DFG/FUGG grant nos. INST 144/379-1 and INST 144/493-1. We acknowledge the use of the EDGAR database developed by the European Commission Joint Research Centre. M. Vojta and N. Gialesakis were supported by the Edu4ClimAte program, funded by the European Commission (Horizon Europe) under grant agreement number 101071247. Andreas Stohl received funding from the European Union's Horizon Europe research and innovation program under grant agreement number 101183460 (IM4CA project). M. Vojta and Andreas Stohl were supported by ClimateLENS – KlimaBLICK, a co-funded research project under the FFG Austrian Space Application Program (ASAP25).

Code and data availability. The TROPOMI/WFMD methane retrievals, along with the corresponding documentation, are publicly available from the University of Bremen at https://www.iup.uni-bremen.de/carbon_ghg/products/tropomi_wfmd/ (Schneising et al., 2020, 2023). CAMS global greenhouse gas reanalysis EGG4 can be downloaded from https://doi.org/10.24381/cda4ed31 (Agustí-Panareda et al., 2023). The FLEXINVERT and FLEXPART codes used for this study are available from the GitLab repository: https://git.nilu.no/flexpart/ and from https://doi.org/10.25365/phaidra.753 (Thompson et al., 2025).

Author contributions. MV designed the study with input from AS and MK, RS generated a priori emission data, RS and RT helped with the inversion setup, RT and MV designed new methods regarding super observations aggregation, NG helped with sattelite data, MV wrote the text with contributions from AS, RT, MK, NG, and RS.

https://doi.org/10.5194/egusphere-2026-3792
Preprint. Discussion started: 21 July 2026

Competing interests. Maria Kanakidou is a member of the editorial board of Atmospheric Chemistry and Physics.

Appendix A: Sensitivity to the baseline optimization

Figure A1 shows the baseline optimization scaling factors for the three vertical layers (panels) and latitudinal bands (colored lines) where initial conditions were optimized. In general, larger adjustments are found in the upper layers compared to the lowest layer. This likely reflects the larger biases in the EGG4 initial mole fraction fields at greater heights, particularly in the stratosphere, where the prescribed CH_4 loss rates were found to be problematic (Agustí-Panareda et al., 2023). In general, negligible adjustments are found for the latitude bands between 90° and 30°S, whereas factors are predominantly larger than unity for 30°S–0° and mostly smaller than unity between 30° and 90°N. The adjustments show similarities and are of comparable magnitude to those reported by Thompson et al. (2025). However, their inversions exhibited substantially larger adjustments in the lowest layer compared to ours, particularly for 30°–90°N, to which their study region, Siberia, was more sensitive.

To assess the impact of the uncertainty assigned to the baseline optimization factors, we test a wide range of values from 0.1% to 7%. Figures S14–S16 summarize the results across this range. Figure S14 shows the same optimized scaling factors as shown in Fig. A1, but for the tested baseline uncertainty values, Figure S15 presents the corresponding a posteriori emissions and inversion increments, and Figure S16 displays the total a posteriori emissions for the EMME region.

For very small uncertainties, optimization scalars remain close to unity, as expected due to the strong constraint imposed by the initial mole fraction field. Consequently, the inversion compensates mismatches between modeled and observed column mole fraction through large and spatially widespread emission increments. In some regions with limited observational coverage, such as Romania, substantial negative increments occur not only at the grid-cell level but across larger areas, likely indicating biases in the initial mole fraction fields that propagate into the a posteriori emissions.

As the assumed uncertainty increases, optimization scalars systematically deviate stronger from unity, while the emission increments become less pronounced. Between 1.3% and 2% uncertainty, scalars show little further change and posterior emissions appear very stable, suggesting a range in which the solution is less sensitive to the exact baseline uncertainty choice. For uncertainties beyond this range, emission increments are progressively reduced as baseline uncertainty increases, and the total a posteriori emissions systematically shift towards the a priori value. Note that all increments preserve their sign across the tested baseline uncertainties, except for a region in eastern Saudi Arabia, where the increment changes from positive to negative as the assumed uncertainty increases. Despite a substantial error reduction, this introduces additional uncertainty in the posterior emissions for Saudi Arabia. For the largest tested uncertainty (7%), significant increments remain only in regions around the Persian Gulf, likely reflecting a strong bias in the a priori emissions, that is corrected across all tested cases.

This observed behavior differs substantially from inversions based on ground-based measurements, where Vojta et al. (2025) showed for the example of SF_6, that posterior emissions converge toward stable values once a certain baseline uncertainty threshold is reached, thus rendering an uncertainty overestimation less critical. However, ground-based measurements (from non-background stations) typically exhibit pronounced concentration peaks that can only be explained by nearby or regional emissions, and not by changes of the initial conditions. This leads to a clearer separation between baseline contributions and

https://doi.org/10.5194/egusphere-2026-3792
Preprint. Discussion started: 21 July 2026

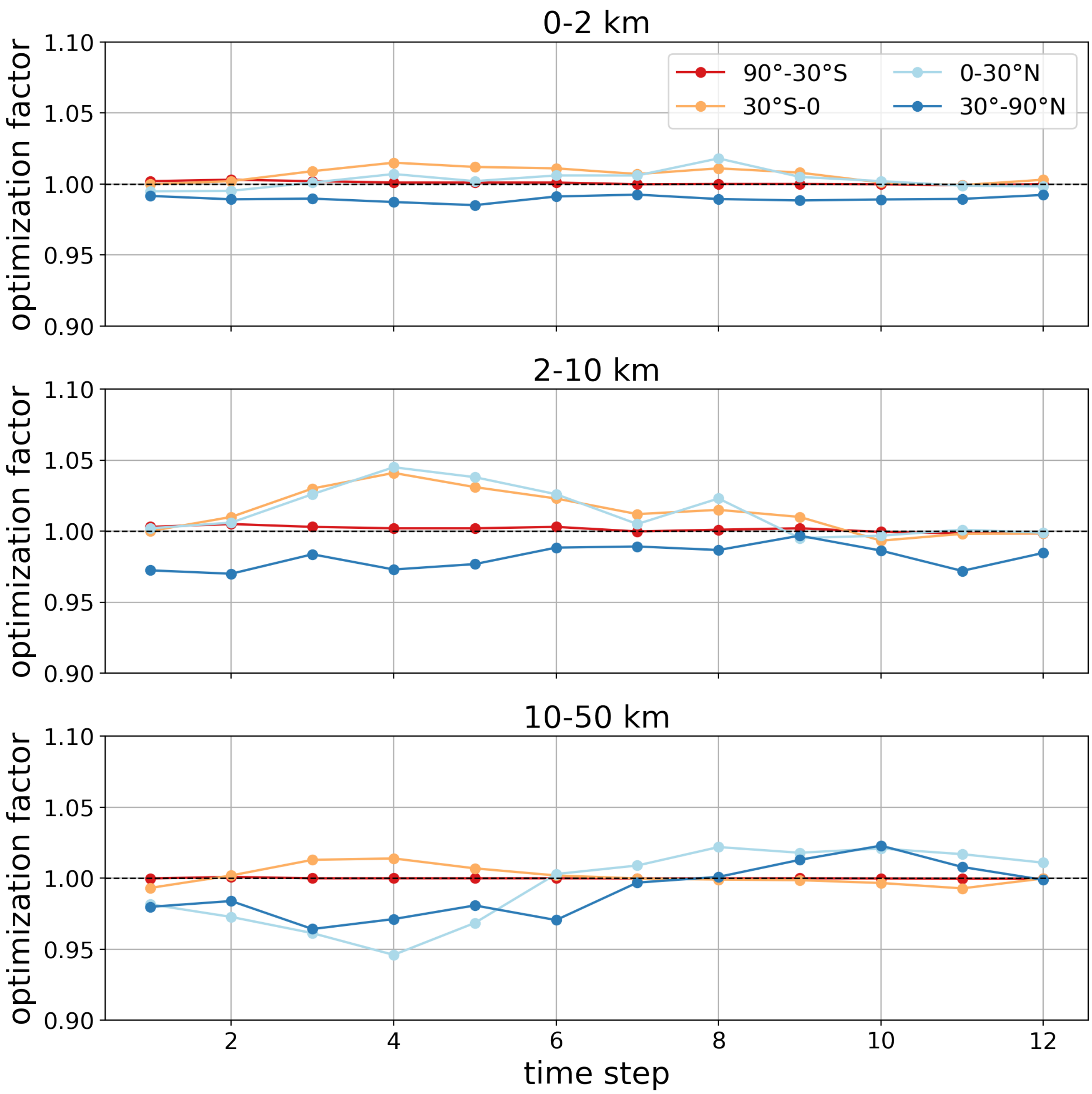

Figure A1. Optimized monthly baseline scaling factors, shown for the individual vertical layers (panels) and latitudinal bands (colored lines)

regional emission signals. As a result, regional emissions are less affected when additional freedom is given to adjust the baseline. In contrast, emission sensitivities for column observations are much more spatially dispersed than for ground-based observations, because column mixing ratios represent contributions from a wide area. Thus, the influence of emissions and initial mixing ratios on column observations is less well spatially separated than for ground observations. Therefore, variations in the observed column mole fractions can be reproduced almost equally well either by changes in regional emissions or by

https://doi.org/10.5194/egusphere-2026-3792
Preprint. Discussion started: 21 July 2026

adjustments to the baseline. If the baseline uncertainty is overestimated, such adjustments may artificially compensate for changes in surface emissions, potentially shifting a posteriori closer to a priori emissions, preventing convergence toward a stable solution.

As a consequence, the baseline uncertainty emerges as a critical parameter. It must be chosen large enough to correct for biases in the initial mole fraction fields, yet small enough to avoid artificially compensating for errors in surface emissions. Determining an appropriate range therefore requires identifying a transition between these two regimes. To investigate this, we rearrange Fig. S14 to illustrate the evolution of the optimized scaling factors as a function of increasing baseline uncertainty, with individual time steps indicated by different colors (Fig A2). We hypothesize that a transition can be identified at a range where the scaling factor adjustments have ceased to increase systematically with increasing uncertainty, indicating that biases in the initial fields are largely corrected. Indeed, a distinct transition range can be identified between 1.3% and 2.0% for our case, indicated by the dashed vertical lines in Fig. A2. This range coincides with the range where total EMME a posteriori emissions remain stable, before they begin to systematically shift towards the prior (Fig. S16). At the same time, obvious artifacts in the gridded a posteriori emission fields have disappeared, while coherent increment patterns remain visible (Fig. S15). While we acknowledge that the chosen baseline uncertainty must remain physically meaningful, and that an estimation from Fig. A2 introduces some subjectivity, we argue that the combination of the presented behaviors provides strong evidence for a transition between effective bias correction and the onset of compensation effects. Finally, we note that the observed behavior may not be universally applicable to all LPDM- and satellite-based inversions, as it likely depends on the magnitude of biases in the initial mole-fraction fields. For cases with smaller initial biases, convergence of the inversion results with increasing baseline uncertainty may still be achieved.

https://doi.org/10.5194/egusphere-2026-3792
Preprint. Discussion started: 21 July 2026

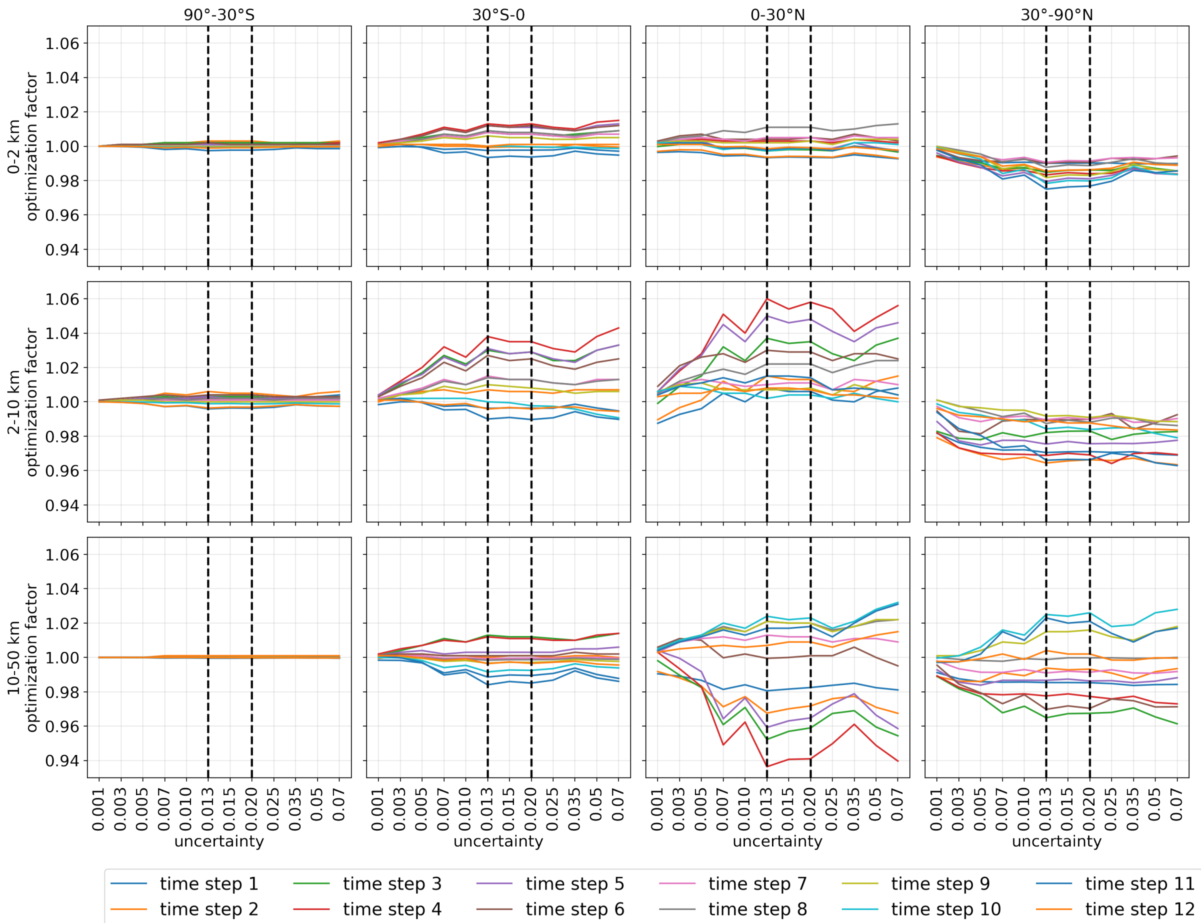

Figure A2. Optimized baseline scalars for all optimization grid cells, shown as a function of multiple baseline uncertainties between 0.1% and 7% and for different optimization time steps (colored lines). The vertical dashed lines are interpreted as the transition zone between effective bias correction and the onset of compensation effects

https://doi.org/10.5194/egusphere-2026-3792
Preprint. Discussion started: 21 July 2026

Appendix B: Sensitivity to the a priori emission errors

A priori emission errors are specified as a fraction of the corresponding emission values in each grid cell, implicitly assuming that regions with higher reported emissions also carry proportionally larger uncertainties. We test five different uncertainty values ranging from 0.3 to 2.0. The resulting total EMME a posteriori emissions are shown in Fig. S17, while Fig.B1 illustrates the spatial distribution of the inversion increments and the corresponding a posteriori emissions. As expected, the inversion increments become more pronounced with increasing emission uncertainty, and the total a posteriori emissions deviate further from the a priori values, as the emissions are less strongly constrained by the prior. However, the inversion increments obtained with low emission uncertainties appear very similar to those found in cases with high baseline uncertainty (see lower panels in Fig. S15 compared to upper panels in Fig. B1), and vice versa. When emissions are strongly constrained by their a priori values (low emission uncertainty), differences between modeled and observed column mole fractions are mainly reduced by baseline corrections rather than emission adjustments, similar to the case of high baseline uncertainty. Conversely, when a priori emission uncertainties are large, the mismatch is predominantly reduced by emission adjustments instead of baseline corrections, analogous to the case of low baseline uncertainty.

Indeed, the discussed transition between effective baseline bias correction and the onset of compensation effects is sensitive to the chosen a priori emission uncertainty, as it likewise influences the balance between emission and baseline adjustments. Figs. S18–S20 show, that for smaller emission uncertainties of 50%, the transition occurs already at lower baseline uncertainties. Notice that the gridded a posteriori emissions, inversion increments, and total emissions are very similar at the transition zones, despite using different a priori uncertainties.

https://doi.org/10.5194/egusphere-2026-3792
Preprint. Discussion started: 21 July 2026

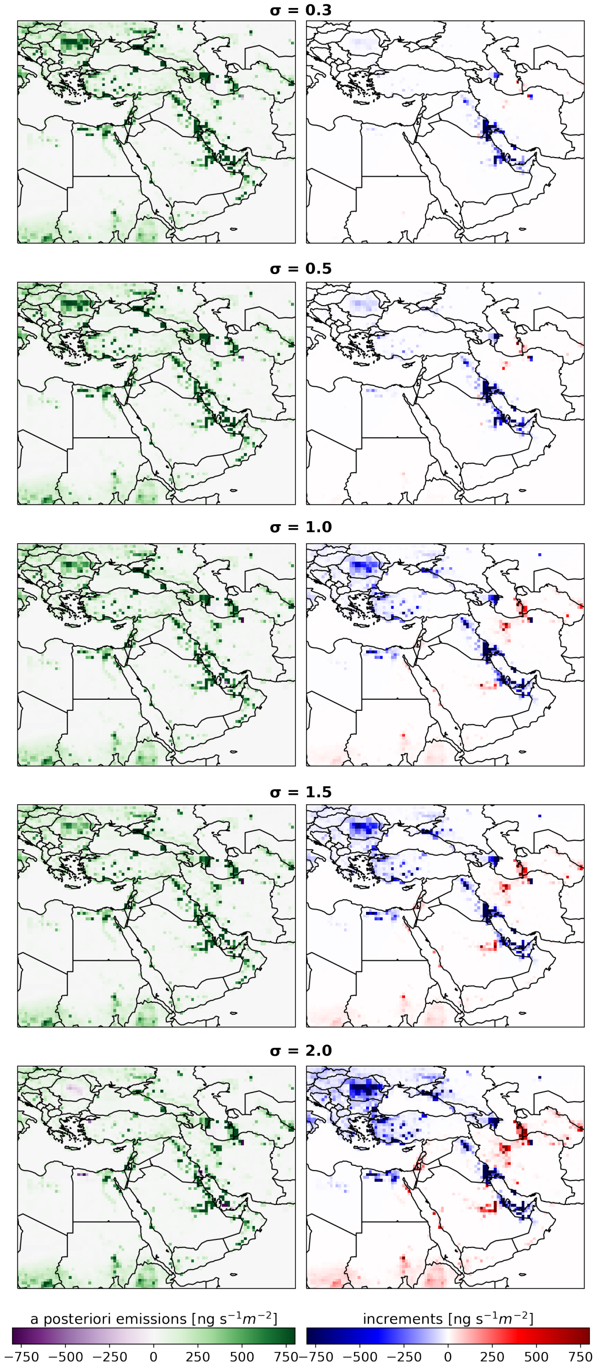

Figure B1. A posteriori emissions and inversion increments, shown for multiple a priori errors between 30% and 200%.

https://doi.org/10.5194/egusphere-2026-3792
Preprint. Discussion started: 21 July 2026

Appendix C: Sensitivity to the spatial correlation length

We test spatial correlation lengths ranging from 50 to 500 km. Figure C1 shows the corresponding total a posteriori emissions, while Fig. S21 illustrates the spatial distribution of the inversion increments and the resulting a posteriori emissions. Similar to Vojta et al. (2025), we find that the inversion increments become more pronounced and extend over larger areas as the correlation length increases, leading to larger deviations of the total a posteriori emissions from the prior. This behavior arises because larger correlation lengths allow observational information to influence a greater number of emission grid cells, effectively increasing the total prior emission uncertainty and enabling larger adjustments.

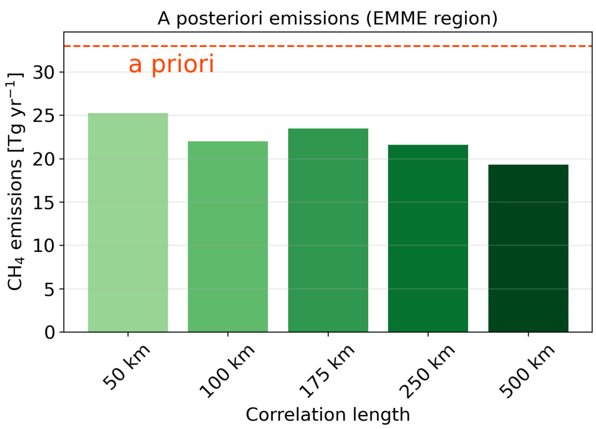

Figure C1. Total a posteriori emissions in the EMME region shown for multiple spatial a priori emission uncertainty correlations between 50 km and 500 km.

Similar to Sect. B we note that the increments obtained with a correlation length of 500 km appear very similar to those found in cases with very low baseline uncertainty. Increasing the correlation length strengthens the effective observation constraint on emissions, so that differences between modeled and observed column mole fractions are predominantly explained by emission adjustments rather than by baseline corrections, similar to the situation when the assumed baseline uncertainty is small. To further investigate this relationship, Fig. S22 shows the evolution of the optimization factor with increasing baseline uncertainty for the case of 500 km correlation length. In this case, the baseline factors continue to increase systematically up to 2%, instead of reaching a plateau at 1.3% for 100 km, suggesting that the stronger emission constraint associated with larger correlation lengths shifts the balance between emission and baseline adjustments.

Appendix D: Sensitivity to the temporal correlation length

We test temporal correlation lengths of 30, 90, and 180 days. Figure D1 shows the corresponding monthly time series of total emissions in the EMME region, while Fig. S23 presents the annual averages for the tested cases. As the temporal correlation length increases, the monthly time series becomes noticeably smoother and loses variability, such that the peak in August can

https://doi.org/10.5194/egusphere-2026-3792
Preprint. Discussion started: 21 July 2026

no longer be resolved for the 90 and 180 days correlation lengths. The annual average results are very similar, however show slightly larger deviations from the a priori emissions as temporal correlation increases and observational information is spread over a larger number of optimization time steps.

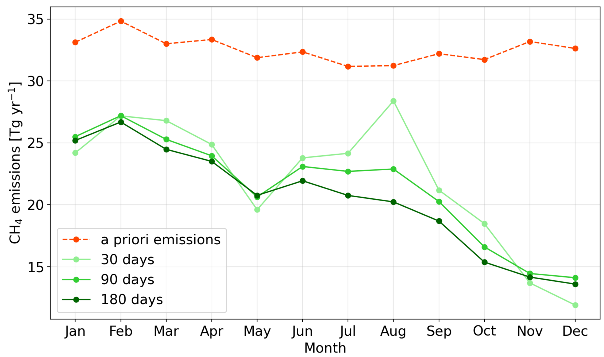

Figure D1. Time series of monthly a posteriori emissions for the entire EMME region, shown for temporal correlation lengths of 30, 90, and 180 days.

Appendix E: Sensitivity to the a priori emisisons

As shown in the main text (Fig. 6), the inversions results in similar posterior emission estimates for Iran, Iraq, Egypt, Turkey, and the total EMME region, even when a priori emissions are very different. However, for Saudi Arabia, the inversion shifts emissions to higher values by a similar absolute amount in all cases and the discrepancies in the prior emissions largely persist, resulting in less certain posterior estimates. This behavior can likely be explained by the definition of the a priori uncertainties as a fraction of the respective emission values, which may provide the inversion algorithm with too little freedom to accommodate large adjustments required for low a priori values. However, it may also reflect the stronger sensitivity to the assumed baseline uncertainty discussed in Sect. A, which generally makes the inversion results for Saudi Arabia less robust.

Appendix F: Lognormal a priori emission distribution

Figure F1 shows the a posteriori emissions and inversion increments obtained using a lognormal a priori error distribution, while Fig. S24 presents the total a posteriori emissions for the major emitting countries and for the entire EMME region. Overall, the resulting emission pattern is consistent with that obtained using a normal a priori distribution. In particular, very similar, strongly negative increments around the Persian Gulf are obtained, while almost identical total a posterior emissions are calculated for Iran and Iraq compared to the normal distribution case. Also the total emission in the EMME region remains very similar across tested case using different priors, underlining the robustness of our results. However, in regions with less error reduction (Fig. 5), the negative increments are less pronounced, such as in Turkey and Egypt. As a result, differences between

https://doi.org/10.5194/egusphere-2026-3792
Preprint. Discussion started: 21 July 2026

a priori inventories are reduced less strongly by the inversion than in the case of a normal a priori distribution. This behavior might be explained by the properties of the lognormal distribution, which is skewed toward higher values and therefore large reductions relative to the prior are penalized more strongly by the inversion. This different behavior is particularly pronounced
630 toward the end of the study period, where the observational data suggest strong negative adjustments (see Fig. S25).

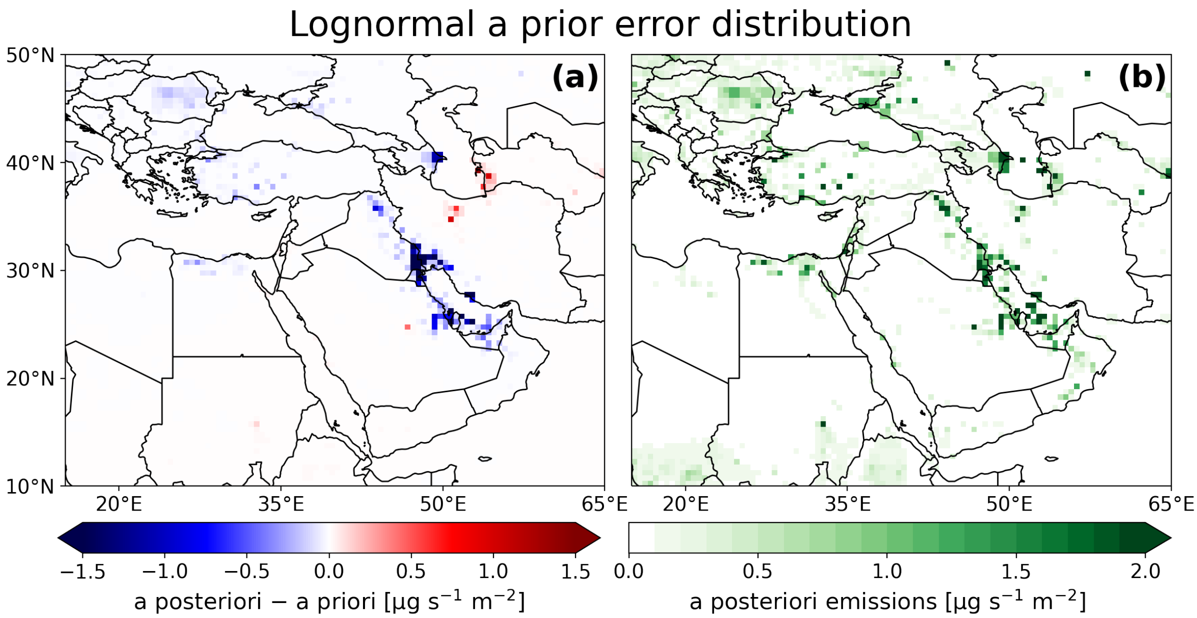

Figure F1. (a) A posteriori emissions and (b) inversion increments when using a lognormal a priori error distribution in the optimization.

References

Agustí-Panareda, A., Barré, J., Massart, S., Inness, A., Aben, I., Ades, M., Baier, B. C., Balsamo, G., Borsdorff, T., Bousserez, N., Boussetta, S., Buchwitz, M., Cantarello, L., Crevoisier, C., Engelen, R., Eskes, H., Flemming, J., Garrigues, S., Hasekamp, O., Huijnen, V., Jones, L., Kipling, Z., Langerock, B., McNorton, J., Meilhac, N., Noël, S., Parrington, M., Peuch, V.-H., Ramonet, M., Razinger, M., Reuter, M., Ribas, R., Suttie, M., Sweeney, C., Tarniewicz, J., and Wu, L.: Technical note: The CAMS greenhouse gas reanalysis from 2003 to 2020, Atmospheric Chemistry and Physics, 23, 3829–3859, https://doi.org/10.5194/acp-23-3829-2023, 2023.

Al Jazeera: Iran cuts oil production to lowest in 40 years as storage fills, https://www.aljazeera.com/economy/2020/7/7/iran-cuts-oil-production-to-lowest-in-40-years-as-storage-fills, accessed: 2026-03-20, 2020.

Baciu, C., Ionescu, A., and Etiope, G.: Hydrocarbon seeps in Romania: gas origin and release to the atmosphere, Marine and Petroleum Geology, 89, 130–143, https://doi.org/10.1016/j.marpetgeo.2017.06.015, 2018.

Bergamaschi, P., Frankenberg, C., Meirink, J. F., Krol, M., Villani, M. G., Houweling, S., Dentener, F., Dlugokencky, E. J., Miller, J. B., Gatti, L. V., et al.: Inverse modeling of global and regional CH4 emissions using SCIAMACHY satellite retrievals, Journal of Geophysical Research: Atmospheres, 114, https://doi.org/10.1029/2009JD012287, 2009.

Bourtsoukidis, E., Germain-Piaulenne, E., Gros, V., Quéhé, P.-Y., Pikridas, M., Byron, J., Williams, J., Gliddon, D., Mohamed, R., Ekaabi, R., et al.: Attribution of excess methane emissions over marine environments of the Mediterranean and Arabian Peninsula, Journal of Geophysical Research: Atmospheres, 129, e2024JD041 621, https://doi.org/10.1029/2024JD041621, 2024.

Chen, Z., Jacob, D. J., Gautam, R., Omara, M., Stavins, R. N., Stowe, R. C., Nesser, H., Sulprizio, M. P., Lorente, A., Varon, D. J., et al.: Satellite quantification of methane emissions and oil–gas methane intensities from individual countries in the Middle East and North Africa: implications for climate action, Atmospheric Chemistry and Physics, 23, 5945–5967, https://doi.org/10.5194/acp-23-5945-2023, 2023.

Copernicus Atmosphere Monitoring Service: CAMS Global Greenhouse Gas Reanalysis (EGG4), https://doi.org/10.24381/cda4ed31, accessed: 2026-06-01, 2021.

Cozzi, A., Assecondi, L., Brandolese, S., Cascone, A., Cornaggia, F., Giovannelli, A., Guarnieri, P., Minervini, M., Ronchi, S. M. P., Ruspi, R., et al.: Zohr giant gas discovery—A paradigm shift in Nile Delta and East Mediterranean exploration, 106, 405–431, https://doi.org/10.1306/13742365MGF.14.3881, 2021.

Crippa, M., D., G., Pagani, F., Banja, M., Muntean, M., E., S., Becker, W., Monforti-Ferrario, F., Quadrelli, R., Risquez Martin, A., Taghavi-Moharamli, P., Köykkä, J., Grassi, G., Rossi, S., Brandao De Melo, J., Oom, D., Branco, A., San-Miguel, J., and Vignati, E.: GHG emissions of all world countries, Publications Office of the European Union, Luxembourg, 2023, https://doi.org/10.2760/953322, 2023.

Crippa, M., Guizzardi, D., Pagani, F., Banja, M., Muntean, M., et al.: GHG Emissions of All World Countries – 2025 Report, https://doi.org/10.2760/9816914, 2025.

Cui, Y., Brioude, J., McKain, K., Kim, J., Frost, G. J., Ahmadov, R., Peischl, J., Ryerson, T. B., Trainer, M., Nehrkorn, T., et al.: Inversion estimates of lognormally distributed methane emission rates from the Haynesville–Bossier oil and gas production region using airborne measurements, Journal of Geophysical Research: Atmospheres, 123, 3515–3532, https://doi.org/10.1002/2017JD027676, 2018.

Cusworth, D. H., Duren, R. M., Thorpe, A. K., Olson-Duvall, W., Heckler, J., Chapman, J. W., Eastwood, M. L., Helmlinger, M. C., Green, R. O., Asner, G. P., et al.: Intermittency of large methane emitters in the Permian Basin, Environmental Science & Technology Letters, 8, 567–573, https://doi.org/10.1021/acs.estlett.1c00173, 2021.

https://doi.org/10.5194/egusphere-2026-3792
Preprint. Discussion started: 21 July 2026

Cusworth, D. H., Thorpe, A. K., Ayasse, A. K., Stepp, D., Heckler, J., Asner, G. P., Miller, C. E., Yadav, V., Chapman, J. W., Eastwood, M. L., et al.: Strong methane point sources contribute a disproportionate fraction of total emissions across multiple basins in the United States, Proceedings of the National Academy of Sciences, 119, e2202338 119, 2022.

Forster, P., Storelvmo, T., Armour, K., Collins, W., Dufresne, J. L., Frame, D., Lunt, D. J., Mauritsen, T., Palmer, M. D., Watanabe, M., Wild, M., and Zhang, H.: The Earth's Energy Budget, Climate Feedbacks, and Climate Sensitivity, in: Climate Change 2021: The Physical Science Basis. Contribution of Working Group I to the Sixth Assessment Report of the Intergovernmental Panel on Climate Change, edited by: Masson-Delmotte, V., Zhai, P., Pirani, A., Connors, S. L., Pean, C., Berger, S., Caud, N., Chen, Y., Goldfarb, L., Gomis, M. I., Huang, M., Leitzell, K., Lonnoy, E., Matthews, J. B. R., Maycock, T. K., Waterfield, T., Yelekci, O., Yu, R., and Zhou, B., Cambridge University Press, Cambridge, UK, https://doi.org/10.1017/9781009157896.009, 2021.

Gialesakis, N., Kalivitis, N., Kouvarakis, G., Ramonet, M., Lopez, M., Kwok, C. Y., Narbaud, C., Daskalakis, N., Mermigkas, M., Mihalopoulos, N., and Kanakidou, M.: A Twenty Year Record of Greenhouse Gases in the Eastern Mediterranean Atmosphere, Science of The Total Environment, 864, 161 003, https://doi.org/10.1016/j.scitotenv.2022.161003, 2023.

Gilbert, J. C. and Lemaréchal, C.: The module M1QN3, INRIA Rep., version, 3, 21, https://who.paris.inria.fr/Jean-Charles.Gilbert/preprint/u01-m1qn3.pdf, last accessed: 2025-02-29, 2006.

Hersbach, H., de Rosnay, P., Bell, B., Schepers, D., Simmons, A., Soci, C., Abdalla, S., Alonso-Balmaseda, M., Balsamo, G., Bechtold, P., Berrisford, P., Bidlot, J.-R., de Boisséson, E., Bonavita, M., Browne, P., Buizza, R., Dahlgren, P., Dee, D., Dragani, R., Diamantakis, M., Flemming, J., Forbes, R., Geer, A., Haiden, T., Hólm, E., Haimberger, L., Hogan, R., Horányi, A., Janiskova, M., Laloyaux, P., Lopez, P., Munoz-Sabater, J., Peubey, C., Radu, R., Richardson, D., Thépaut, J.-N., Vitart, F., Yang, X., Zsótér, E., and Zuo, H.: Operational global reanalysis: progress, future directions and synergies with NWP, https://doi.org/10.21957/tkic6g3wm, series: ERA Report, 2018.

IEA: Global Energy Review 2020, Tech. rep., International Energy Agency, Paris, https://www.iea.org/reports/global-energy-review-2020, licence: CC BY 4.0, 2020.

IEA: International Energy Agency: World Energy Balances: Overview, https://www.iea.org/reports/world-energy-balances-overview/middle-east, licence: CC BY 4.0, Last accessed: 18 March 2026, 2021.

IEA: International Energy Agency: Global Methane Tracker 2024, https://www.iea.org/reports/global-methane-tracker-2024, licence: CC BY 4.0, Last accessed: 18 March 2025, 2024.

Irakulis-Loitxate, I., Guanter, L., Liu, Y.-N., Varon, D. J., Maasakkers, J. D., Zhang, Y., Chulakadabba, A., Wofsy, S. C., Thorpe, A. K., Duren, R. M., et al.: Satellite-based survey of extreme methane emissions in the Permian basin, Science Advances, 7, eabf4507, https://doi.org/10.1126/sciadv.abf4507, 2021.

Jacob, D. J., Varon, D. J., Cusworth, D. H., Dennison, P. E., Frankenberg, C., Gautam, R., Guanter, L., Kelley, J., McKeever, J., Ott, L. E., et al.: Quantifying methane emissions from the global scale down to point sources using satellite observations of atmospheric methane, Atmospheric Chemistry and Physics, 22, 9617–9646, https://doi.org/10.5194/acp-22-9617-2022, 2022.

Karcz, K., Gellman, Y., Shitrit, O., and Steinberg, J.: The leviathan field-Nine years since discovery and nearing first gas, in: Second EAGE Eastern Mediterranean Workshop, vol. 2019, pp. 1–5, European Association of Geoscientists & Engineers, https://doi.org/10.3997/2214-4609.201903152, 2019.

Kayrros: U.S. Methane Emissions from Fossil Fuels at Risk of Worsening in 2022, Tech. rep., Kayrros, https://www.energy.gov/sites/default/files/2023-05/Attachment%20BB%20-%20Kayrros%20-%20Methane%20Emissions%20Worsening.pdf, attachment BB in U.S. DOE docket, 2022.

Kivimäki, E., Tenkanen, M., Aalto, T., Buchwitz, M., Luojus, K., Pulliainen, J., Rautiainen, K., Schneising, O., Sundström, A.-M., Tamminen, J., Tsuruta, A., and Lindqvist, H.: Environmental drivers constraining the seasonal variability in satellite-observed and modelled methane at northern high latitudes, Biogeosciences, 22, 5193–5230, https://doi.org/10.5194/bg-22-5193-2025, 2025.

Lan, X., Thoning, K., and Dlugokencky, E.: Trends in globally-averaged CH_4, N_2O, and SF_6 determined from NOAA Global Monitoring Laboratory measurements, https://doi.org/10.15138/P8XG-AA10, 2025.

Lelieveld, J., Berresheim, H., Borrmann, S., Crutzen, P. J., Dentener, F. J., Fischer, H., Feichter, J., Flatau, P. J., Heland, J., Holzinger, R., Kormann, R., Lawrence, M. G., Levin, Z., Markowicz, K. M., Mihalopoulos, N., Minikin, A., Ramanathan, V., De Reus, M., Roelofs, G. J., Scheeren, H. A., Sciare, J., Schlager, H., Schultz, M., Siegmund, P., Steil, B., Stephanou, E. G., Stier, P., Traub, M., Warneke, C., Williams, J., and Ziereis, H.: Global Air Pollution Crossroads over the Mediterranean, 298, 794–799, https://doi.org/10.1126/science.1075457, 2002.

Lin, J. C.: Lagrangian Modeling of the Atmosphere: An Introduction, American Geophysical Union, https://doi.org/10.1029/2012GM001376, 2012.

Lyon, D. R., Hmiel, B., Gautam, R., Omara, M., Roberts, K. A., Barkley, Z. R., Davis, K. J., Miles, N. L., Monteiro, V. C., Richardson, S. J., Conley, S., Smith, M. L., Jacob, D. J., Shen, L., Varon, D. J., Deng, A., Rudelis, X., Sharma, N., Story, K. T., Brandt, A. R., Kang, M., Kort, E. A., Marchese, A. J., and Hamburg, S. P.: Concurrent variation in oil and gas methane emissions and oil price during the COVID-19 pandemic, Atmospheric Chemistry and Physics, 21, 6605–6626, https://doi.org/10.5194/acp-21-6605-2021, 2021.

McNorton, J., Bousserez, N., Agustí-Panareda, A., Balsamo, G., Cantarello, L., Engelen, R., Huijnen, V., Inness, A., Kipling, Z., Parrington, M., et al.: Quantification of methane emissions from hotspots and during COVID-19 using a global atmospheric inversion, Atmospheric Chemistry and Physics, 22, 5961–5981, https://doi.org/10.5194/acp-22-5961-2022, 2022.

Mousavi, S. M., Dinan, N. M., Ansarifard, S., Borhani, F., Darvishi, A., Mustafa, F., and Naghibi, A.: Unveiling the drivers of atmospheric methane variability in Iran: A 20-year exploration using spatiotemporal modeling and machine learning, Environmental Challenges, 15, 100 946, https://doi.org/10.1016/j.envc.2024.100946, 2024.

Nisbet, E., Fisher, R., Lowry, D., France, J., Allen, G., Bakkaloglu, S., Broderick, T., Cain, M., Coleman, M., Fernandez, J., et al.: Methane mitigation: methods to reduce emissions, on the path to the Paris agreement, Reviews of Geophysics, 58, e2019RG000 675, https://doi.org/10.1029/2019rg000675, 2020.

Ocko, I. B., Sun, T., Shindell, D., Oppenheimer, M., Hristov, A. N., Pacala, S. W., Mauzerall, D. L., Xu, Y., and Hamburg, S. P.: Acting Rapidly to Deploy Readily Available Methane Mitigation Measures by Sector Can Immediately Slow Global Warming, Environmental Research Letters, 16, 054 042, https://doi.org/10.1088/1748-9326/abf9c8, 2021.

Paris, J.-D., Riandet, A., Bourtsoukidis, E., Delmotte, M., Berchet, A., Williams, J., Ernle, L., Tadic, I., Harder, H., and Lelieveld, J.: Shipborne measurements of methane and carbon dioxide in the Middle East and Mediterranean areas and contribution from oil and gas emissions, Atmospheric Chemistry and Physics Discussions, 2021, 1–28, https://doi.org/10.5194/acp-21-12443-2021, 2021.

Ricaud, P., Zbinden, R., Catoire, V., Brocchi, V., Dulac, F., Hamonou, E., Canonici, J.-C., El Amraoui, L., Massart, S., Piguet, B., et al.: The GLAM airborne campaign across the Mediterranean Basin, Bulletin of the American Meteorological Society, 99, 361–380, https://doi.org/10.1175/BAMS-D-16-0226.1, 2018.

Rigby, M., Prinn, R. G., Fraser, P. J., Simmonds, P. G., Langenfelds, R., Huang, J., Cunnold, D. M., Steele, L. P., Krummel, P. B., Weiss, R. F., et al.: Renewed growth of atmospheric methane, Geophysical research letters, 35, https://doi.org/10.1029/2008GL036037, 2008.

Rijsdijk, P., Eskes, H., Dingemans, A., Boersma, K. F., Sekiya, T., Miyazaki, K., and Houweling, S.: Quantifying Uncertainties in Satellite NO_2 Superobservations for Data Assimilation and Model Evaluation, Geoscientific Model Development, 18, 483–509, https://doi.org/10.5194/gmd-18-483-2025, 2025.

Rodgers, C. D. and Connor, B. J.: Intercomparison of Remote Sounding Instruments, 108, 2002JD002 299, https://doi.org/10.1029/2002JD002299, 2003.

Rosenberg, T. and Nada, G.: Two Years of COVID: Economic Cost, https://iranprimer.usip.org/blog/2022/feb/16/two-years-covid-economic-cost, accessed: 2026-04-02, 2022.

Saunois, M., Martinez, A., Poulter, B., Zhang, Z., Raymond, P. A., Regnier, P., Canadell, J. G., Jackson, R. B., Patra, P. K., Bousquet, P., Ciais, P., Dlugokencky, E. J., Lan, X., Allen, G. H., Bastviken, D., Beerling, D. J., Belikov, D. A., Blake, D. R., Castaldi, S., Crippa, M., Deemer, B. R., Dennison, F., Etiope, G., Gedney, N., Höglund-Isaksson, L., Holgerson, M. A., Hopcroft, P. O., Hugelius, G., Ito, A., Jain, A. K., Janardanan, R., Johnson, M. S., Kleinen, T., Krummel, P. B., Lauerwald, R., Li, T., Liu, X., McDonald, K. C., Melton, J. R., Mühle, J., Müller, J., Murguia-Flores, F., Niwa, Y., Noce, S., Pan, S., Parker, R. J., Peng, C., Ramonet, M., Riley, W. J., Rocher-Ros, G., Rosentreter, J. A., Sasakawa, M., Segers, A., Smith, S. J., Stanley, E. H., Thanwerdas, J., Tian, H., Tsuruta, A., Tubiello, F. N., Weber, T. S., van der Werf, G. R., Worthy, D. E. J., Xi, Y., Yoshida, Y., Zhang, W., Zheng, B., Zhu, Q., and Zhuang, Q.: Global Methane Budget 2000–2020, Earth System Science Data, 17, 1873–1958, https://doi.org/10.5194/essd-17-1873-2025, 2025.

Scarpelli, T. R., Jacob, D. J., Grossman, S., Lu, X., Qu, Z., Sulprizio, M. P., Zhang, Y., Reuland, F., Gordon, D., and Worden, J. R.: Updated Global Fuel Exploitation Inventory (GFEI) for methane emissions from the oil, gas, and coal sectors: evaluation with inversions of atmospheric methane observations, Atmospheric Chemistry and Physics, 22, 3235–3249, https://doi.org/10.5194/acp-22-3235-2022, 2022.

Scarpelli, T. R., Roy, E., Jacob, D. J., Sulprizio, M. P., Tate, R. D., and Cusworth, D. H.: Using New Geospatial Data and 2020 Fossil Fuel Methane Emissions for the Global Fuel Exploitation Inventory (GFEI) V3, Earth System Science Data, 17, 7019–7033, https://doi.org/10.5194/essd-17-7019-2025, 2025.

Schneising, O., Buchwitz, M., Reuter, M., Vanselow, S., Bovensmann, H., and Burrows, J. P.: Remote sensing of methane leakage from natural gas and petroleum systems revisited, Atmospheric Chemistry and Physics, 20, 9169–9182, https://doi.org/10.5194/acp-20-9169-2020, 2020.

Schneising, O., Buchwitz, M., Hachmeister, J., Vanselow, S., Reuter, M., Buschmann, M., Bovensmann, H., and Burrows, J. P.: Advances in retrieving XCH_4 and XCO from Sentinel-5 Precursor: improvements in the scientific TROPOMI/WFMD algorithm, Atmospheric Measurement Techniques, 16, 669–694, https://doi.org/10.5194/amt-16-669-2023, 2023.

Shahzadi, K., Schneider, M., Lo, N. Y., Hase, F., Meyer, J., Cayoglu, U., Borsdorff, T., and Martinez-Velarte, M. C.: A multi-year global methane data set obtained by merging observations from TROPOMI and IASI, Earth System Science Data, 18, 2153–2177, https://doi.org/10.5194/essd-18-2153-2026, 2026.

Shen, L., Zavala-Araiza, D., Gautam, R., Omara, M., Scarpelli, T., Sheng, J., Sulprizio, M. P., Zhuang, J., Zhang, Y., Qu, Z., et al.: Unravelling a large methane emission discrepancy in Mexico using satellite observations, Remote Sensing of Environment, 260, 112 461, https://doi.org/10.1016/j.rse.2021.112461, 2021.

Shen, L., Gautam, R., Omara, M., Zavala-Araiza, D., Maasakkers, J. D., Scarpelli, T. R., Lorente, A., Lyon, D., Sheng, J., Varon, D. J., et al.: Satellite quantification of oil and natural gas methane emissions in the US and Canada including contributions from individual basins, Atmospheric chemistry and physics, 22, 11 203–11 215, https://doi.org/10.5194/acp-22-11203-2022, 2022.

Subramanian, R., Thompson, R. L., Vojta, M., Schneising, O., and Stohl, A.: Strong monsoon influence on South Asian methane emissions in 2020 revealed by a Bayesian inversion constrained by satellite observations, EGUsphere, https://doi.org/10.5194/egusphere-2025-5108, preprint, 2025.

https://doi.org/10.5194/egusphere-2026-3792
Preprint. Discussion started: 21 July 2026

Szopa, S., Naik, V., Adhikary, B., Artaxo, P., Berntsen, T., Collins, W. D., Fuzzi, S., Gallardo, L., Kiendler-Scharr, A., Klimont, Z., Liao, H., Unger, N., and Zanis, P.: Short-Lived Climate Forcers, pp. 817–922, Cambridge University Press, Cambridge, United Kingdom and New York, NY, USA, https://doi.org/10.1017/9781009157896.008, 2021.

Tarantola, A.: Inverse Problem Theory and Methods for Model Parameter Estimation, pp. 1–67, Society for Industrial and Applied Mathematics, https://doi.org/10.1137/1.9780898717921, 2005.

Thompson, R. L. and Stohl, A.: FLEXINVERT: an atmospheric Bayesian inversion framework for determining surface fluxes of trace species using an optimized grid, Geoscientific Model Development, 7, 2223–2242, https://doi.org/10.5194/gmd-7-2223-2014, 2014.

Thompson, R. L., Krishnankutty, N., Pisso, I., Schneider, P., Stebel, K., Sasakawa, M., Stohl, A., and Platt, S. M.: Efficient use of a Lagrangian particle dispersion model for atmospheric inversions using satellite observations of column mixing ratios, Atmospheric Chemistry and Physics, 25, 12 737–12 751, https://doi.org/10.5194/acp-25-12737-2025, 2025.

TradingEconomics.com: Iran crude oil production, https://tradingeconomics.com/iran/crude-oil-production, accessed: 2026-04-02, 2026.

Tsuruta, A., Kivimäki, E., Lindqvist, H., Karppinen, T., Backman, L., Hakkarainen, J., Schneising, O., Buchwitz, M., Lan, X., Kivi, R., et al.: CH_4 Fluxes Derived from Assimilation of TROPOMI XCH_4 in CarbonTracker Europe-CH_4: Evaluation of Seasonality and Spatial Distribution in the Northern High Latitudes, Remote Sensing, 15, 1620, https://doi.org/10.3390/rs15061620, 2023.

Varon, D. J., Jacob, D. J., Hmiel, B., Gautam, R., Lyon, D. R., Omara, M., Sulprizio, M., Shen, L., Pendergrass, D., Nesser, H., et al.: Continuous weekly monitoring of methane emissions from the Permian Basin by inversion of TROPOMI satellite observations, Atmospheric Chemistry and Physics Discussions, 2022, 1–26, https://doi.org/10.5194/acp-23-7503-2023, 2022.

Veefkind, J. P., Aben, I., McMullan, K., Förster, H., de Vries, J., Otter, G., Claas, J., Eskes, H. J., de Haan, J. F., Kleipool, Q., van Weele, M., Hasekamp, O., Hoogeveen, R., Landgraf, J., Snel, R., Tol, P., Ingmann, P., Voors, R., Kruizinga, B., Vink, R., Visser, H., and Levelt, P. F.: TROPOMI on the ESA Sentinel-5 Precursor: A GMES mission for global observations of the atmospheric composition for climate, air quality and ozone layer applications, Remote Sensing of Environment, 120, 70–83, https://doi.org/10.1016/j.rse.2011.09.027, 2012.

Vojta, M., Plach, A., Thompson, R. L., Purohit, P., Stanley, K., O'Doherty, S., Young, D., Pitt, J., Arduini, J., Lan, X., and Stohl, A.: Quantifying European SF_6 emissions from 2005 to 2021 using a large inversion ensemble, Atmospheric Chemistry and Physics, 25, 15 197–15 243, https://doi.org/10.5194/acp-25-15197-2025, 2025.

Vojta, M., Thompson, R. L., and Pisso, I.: Implementation and Evaluation of the Lognormal Prior Probability Distribution in a Variational Atmospheric Inversion Framework, EGUsphere, https://doi.org/10.5194/egusphere-2026-2125, preprint, 2026.

Western, L. M., Ramsden, A. E., Ganesan, A. L., Boesch, H., Parker, R. J., Scarpelli, T. R., Tunnicliffe, R. L., and Rigby, M.: Estimates of North African methane emissions from 2010 to 2017 using GOSAT observations, Environmental Science & Technology Letters, 8, 626–632, https://doi.org/10.1021/acs.estlett.1c00327, 2021.

Williams, J. P., Omara, M., Himmelberger, A., Zavala-Araiza, D., MacKay, K., Benmergui, J., Sargent, M., Wofsy, S. C., Hamburg, S. P., and Gautam, R.: Small emission sources in aggregate disproportionately account for a large majority of total methane emissions from the US oil and gas sector, Atmospheric Chemistry and Physics, 25, 1513–1532, https://doi.org/10.5194/acp-25-1513-2025, 2025.

Worden, J., Cusworth, D., Qu, Z., Yin, Y., Zhang, Y., Bloom, A. A., Ma, S., Byrne, B., Scarpelli, T. R., Maasakkers, J., et al.: The 2019 methane budget and uncertainties at 1 degree resolution and each country through Bayesian integration Of GOSAT total column methane data and a priori inventory estimates, Atmospheric Chemistry and Physics Discussions, 2021, 1–64, https://doi.org/10.5194/acp-22-6811-2022, 2022.

https://doi.org/10.5194/egusphere-2026-3792
Preprint. Discussion started: 21 July 2026

Zhang, Y., Gautam, R., Pandey, S., Omara, M., Maasakkers, J. D., Sadavarte, P., Lyon, D., Nesser, H., Sulprizio, M. P., Varon, D. J., et al.: Quantifying methane emissions from the largest oil-producing basin in the United States from space, Science advances, 6, eaaz5120, https://doi.org/10.1126/sciadv.aaz5120, 2020.